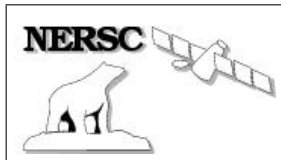


Nansen Environmental and Remote Sensing Center

*A non-profit
environmental research
center affiliated with the
University of Bergen*



*Thormøhlensg. 47
N-5006 Bergen, Norway
Tel: +47 55 20 58 00
Fax: +47 55 20 58 01*

NERSC technical report No. 313

Sea ice model evolution

by

Vincent Vionnet

Summer 2009

Nansen Environmental and Remote Sensing Center (NERSC)

Thormøhlensgate 47

N-5006 Bergen

Norway

phone +47 55205800

fax +47 55205801

email admin@nersc.no

TITLE

Sea Ice Model Evolution

Influence of the snow cover

REPORT IDENTIFICATION

Tech. Rep. 313

CLIENT

CONTRACT NO. 514

CLIENT REFERENCE

AVAILABILITY

AUTHORS

Vincent Vionnet

AUTHORIZATION

Bergen, April 15, 2009

Prof. Ola M. Johannessen
Director NERSC

Contents

1	Sea Ice model in NERSC-HYCOM 2.1	2
1.1	Model presentation	2
1.2	Shortwave radiations..... Daily average cloud cover fraction – 6-hour forcing time step	2
1.3	Snow scheme correction..... Snow depth evolution – Surface temperature of melting snow – Simulations	4
1.4	Comparison with observations.....	6
2	Sea Ice model in NERSC-HYCOM 2.2	8
2.1	Model Overview	8
2.2	Advection scheme	8
2.3	Long-term simulation	9
3	Albedo evolution	14
3.1	Albedo: comparison with observations	14
	Data – Albedo comparison	
3.2	Albedo evolution from SHEBA	17
	Observational data – Description of albedo parameterizations – Albedo evolution	
3.3	Melt ponds evolution	21
	Observations during SHEBA – Ponds evolution modeling – Comparison with observations – Adaptation of melt ponds parameterization	
3.4	Final albedo formulation	24
	Formulation – Comparison with observations	
3.5	Simulations results.....	27
	Configuration – Effects on the sea ice cover	
4	Snow heterogeneities over a grid cell	28
4.1	SSNOWD: a representation of snow cover heterogeneities.....	28
4.2	Snow-depth distribution on sea-ice..... Global distribution – Temporal and spatial evolution	30
4.3	Implementation of SSNOWD in a sea-ice model	35
	SSNOWD in the snow component of ICESTATE – Snow distribution on different ice types – Albedo formulation – Effect on heat transfer	
A	Snow depth distribution (from <i>Iacoza and Barber (1999)</i>)	39

Chapter 1

Sea Ice model in NERSC-HYCOM 2.1

1.1 Model presentation

The model system consists of the HYbrid Coordinate Ocean Model (HYCOM), the Elastic-Viscous-Plastic (EVP) ice dynamics model coupled to a sea-ice model (*Drange and Simonsen, 1996*) describing the thermodynamic evolution of the sea-ice cover. In this chapter the model has a grid size ranging from 50 to 80 km in the North Atlantic and Arctic regions. The ocean time step is set to 15 minutes. The simulation uses reanalysed data ERA40 (*Uppala et al., 2005*) from the European Center for Medium-Range Weather Forecasts (ECMWF). Data used from ERA 40 are temperature at 2 meters, dew-point temperature at 2 meters, wind at 10 meters, cloud cover fraction and precipitation with a temporal resolution of 6 hours.

Several modifications concerning the sea-ice model have been implemented and tested. The results of simulations including those modifications are presented in the following sections.

1.2 Shortwave radiations

The shortwave downward radiation flux Q_{sw}^0 is computed based on *Drange and Simonsen (1996)*. At each time step the daily average value for the given day is used to solve the surface energy budget (over sea ice or over the ocean). Using daily average fluxes allows to reproduce seasonal cycle but not daily cycle of solar radiation. The effect of clouds is included by applying a correction factor based on the cloudiness cc in fractions of unity to the total radiation under clear skies. The cloud cover fraction is taken from ERA 40 forcing fields with a 6-hour time step. The higher is the cloud cover fraction (ranging from 0 to 1), the lower is the shortwave incoming flux.

1.2.1 Daily average cloud cover fraction

The daily average of Q_{sw}^0 is computed at the beginning of each day and kept constant until the next day. In the default version of the model the cloud cover fraction used to compute this flux is given by the ERA 40 field between 00 and 06 am. This value is not necessary representative of the daily average of the cloud cover fraction. That's why we decided to use the daily average instead of the value between 00 and 06 am for the cloud cover fraction.

The effects of this modification are evaluated by comparing the results of two simulations: one with the default version of the model (BAS) and the other with the modified radiation scheme (QAV). Both simulations last 7 years from July 1990 to September 1997.

The difference in monthly average ice-thickness and ice concentration are computed over the Arctic Basin (not shown). No significant trend is observed in the ice thickness and concentration evolution. However this modification enables to compute a more consistent daily average shortwave radiation flux.

1.2.2 6-hour forcing time step

The cloud cover fraction cc is available every six hours from ERA 40 forcing fields. To introduce a reproduction of the diurnal cycle we compute a 6-hour average of Q_{sw}^0 using cc from ERA 40.

Figure 1.1 illustrates the evolution of downward shortwave radiation with and without diurnal cycle. Figure 1.1 (a) shows the amplitude of variations of Q_{sw}^0 around the daily average value with a constant cloud cover fraction ($cc = 1$). When cc is allowed to evolve (Figure 1.1 (b)), the shortwave radiation flux can be twice (for clear skies) as its value with $cc = 1$.

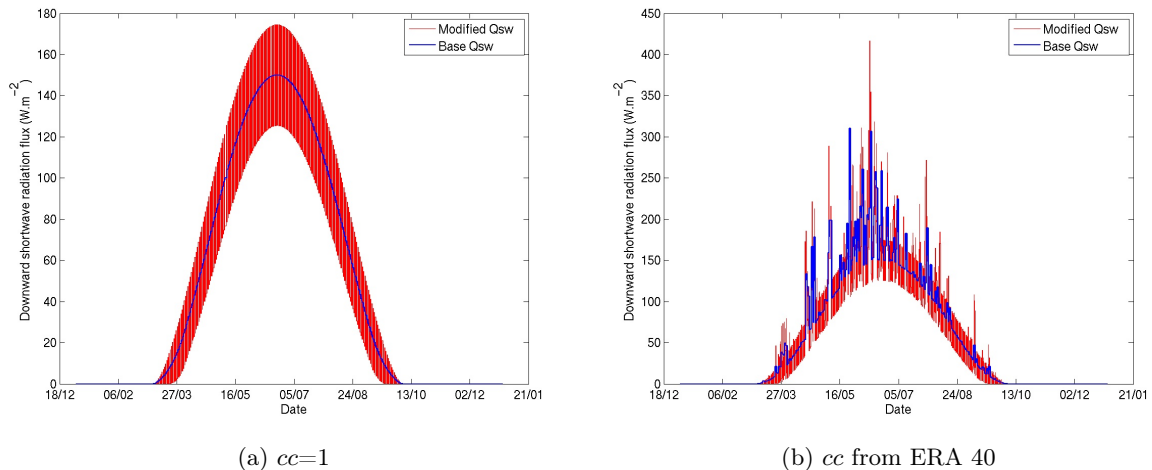


Figure 1.1: Time series of downward shortwave radiation in 1992 at 85N 0W: with diurnal cycle (red) and without diurnal cycle (blue)

The effects of this modification are evaluated at the scale of the Arctic Basin (Figure 1.2). The results from a simulation with the modified radiation scheme (QMD) are compared with the base simulation (BAS). Both simulations start in July 1974 and last 26 years.

The sea ice area coverage difference (figure 1.2 a) shows an annual cycle but its amplitude remains small. Each year the difference is maximal in May. The sea ice volume difference (figure 1.2 b) decreases slowly on average: -0.1% (1975-1979), -1.6% (1980-1989) and -2.3% (1990-1999).

Using a one dimensional thermodynamical sea ice model *Hanesiak et al.* (1999) showed that using hourly or daily average forcing data could change significantly breakup dates (for first-year ice), open water duration and snow ablation. The diurnal distribution of downwelling shortwave energy enhances snow-melt events during hours with higher incoming solar radiation. This effect is not observed in this study with 6-hour radiation data used instead of daily average radiation data.

The default version of the model (BAS) includes a limitation that does not allow the snow albedo to switch to its melting value when snow is melting (see 1.3.2). The positive albedo feedback (higher shortwave radiation absorption due to albedo decrease during diurnal melt events) was identified by *Hanesiak et al.* (1999) as the dominant process that explained snow cover evolution difference between hourly and daily average data. A version of the model allowing the snow albedo to take its melting value (see 1.3.2) is used to perform two simulations: the first with the default radiation scheme, the second using a 6-hour time step for the incoming shortwave radiation flux. The difference between those simulations (not shown) are similar to the observations on figure 1.2. In this configuration of the model the ice albedo feedback does not enhance snow and ice melting when the time step of the radiation scheme is reduced.

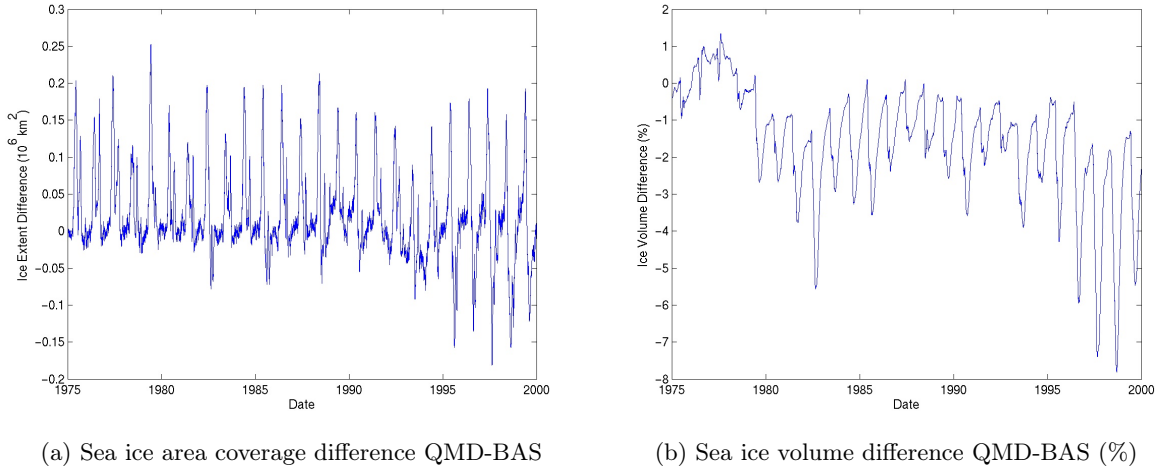


Figure 1.2: Difference of sea ice cover properties over the Arctic basin between experiments QMD and BAS from 1975 to 2000

1.3 Snow scheme correction

Looking into the algorithm of the snow component of the sea ice model showed that physically unrealistic assumptions have been made. They refer to the snow depth evolution and the surface temperature when melting snow is present.

1.3.1 Snow depth evolution

In the default version of the model, snow thicker than 20 cm is assumed to melt. If the snow is dry, 11 cm are removed and enter the ocean through rifts and leads as fresh water. If it is melting snow, the 20 cm of snow are removed in one time step. This never happens in the model because snow is always considered as dry snow (see subsection 1.3.2). This evolution is not physically realistic and leads to unrealistic snow pattern in the Arctic (figure 1.3 (a)).

The snow component is modified as follows. Snow is assumed to be limited in thickness due to wind blowing in into leads and polynya. We put an upper limit on snow thickness equals to 40 cm. This value is consistent with the maximum depth of snow cover on level ice in April in the Arctic Basin published in *Romanov* (1995). When snow depth reaches its maximum value, excess snowfall are supposed to enter directly the ocean as a fresh water input. Snow depth is kept constant to its maximum value until the beginning of the melting period.

Figure 1.3 (b) shows a more regular pattern in snow depth with snow accumulation in the Central Arctic. The pattern on both maps is similar in regions with low snow depth (such as Laptev sea or Baffin Bay).

1.3.2 Surface temperature of melting snow

When snow is melting, its temperature is a constant equals to the melting temperature $T_m = 273.15$ K. In the default version of the model, the surface temperature T_{surf} is below T_m when snow is melting with consequences on the snow albedo value. Indeed *Drange and Simonsen* (1996) used two values to describe snow albedo α_s :

$$\alpha_s(i) = \begin{cases} 0.85 & \text{if } T_{surf} < T_m \\ 0.66 & \text{if } T_{surf} = T_m \end{cases} \quad (1.1)$$

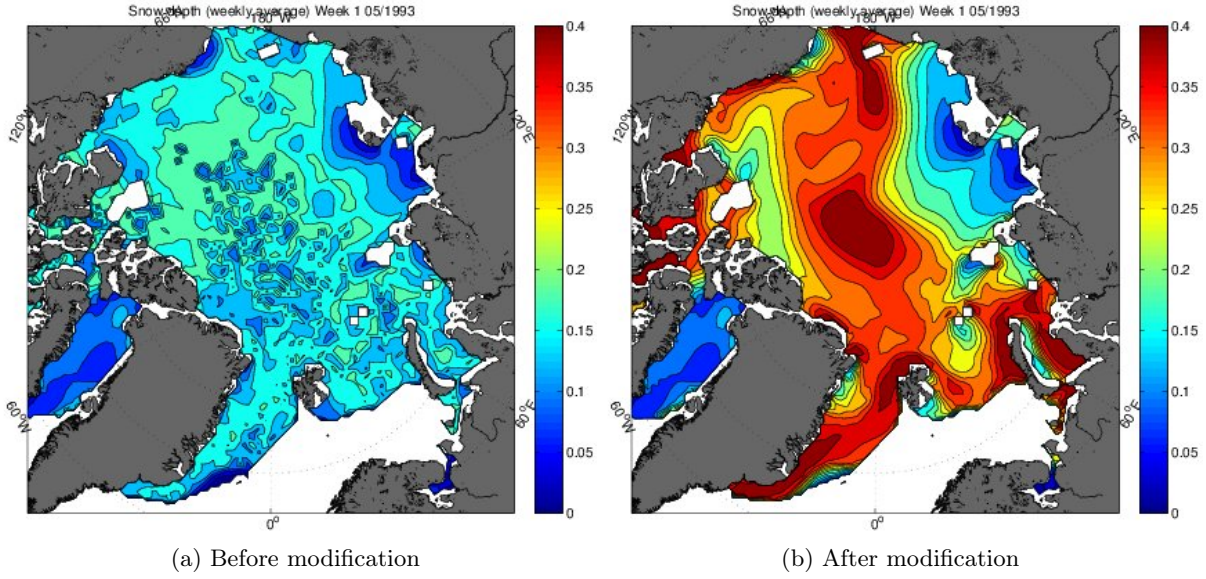


Figure 1.3: Snow depth pattern in the Arctic for the first week of May 1993

As T_{surf} is always lower than T_m , the snow albedo is never equals to its value for melting snow and could lead to wrong estimation of the surface energy budget during the melting period.

The algorithm has been modified to allow T_{surf} to reach T_m during the snow melting period.

1.3.3 Simulations

To estimate the effects of those modifications, the results of two simulations are compared. The first one, named BAS, is run with the default version of the model whereas the second one, named TMD, includes the modifications described in 1.3.1 and 1.3.2. Both simulations start in July 1974 and last 26 years. The initial ice conditions (concentration, thickness) are the same and the meteorological forcing fields are extracted from ERA 40 reanalysis.

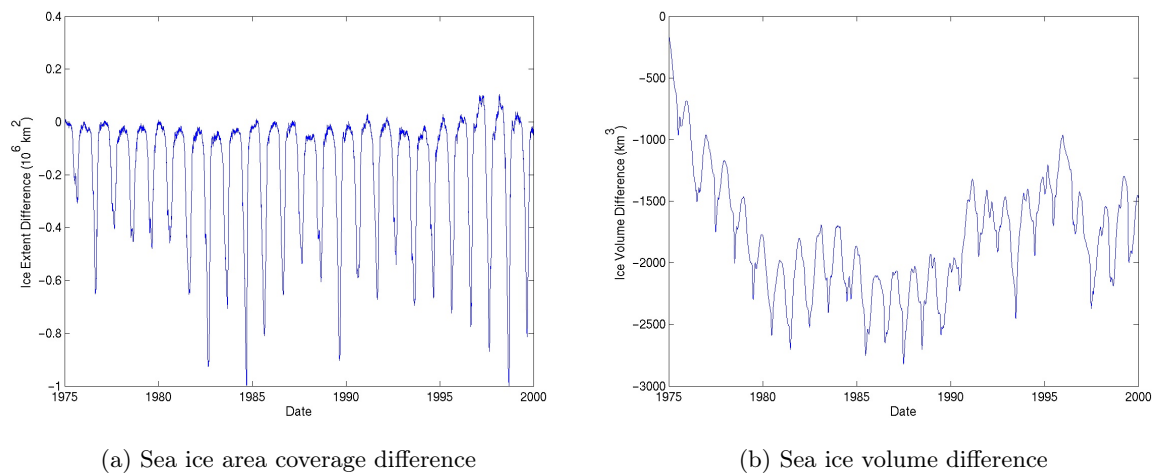


Figure 1.4: Difference of sea ice cover properties between experiments BAS and TMD from 1975 to 2000

The difference of sea ice area coverage and volume between the two experiments are plotted (fig-

ure 1.4). The difference of sea ice area coverage follows an annual cycle. It is around zero during the winter (maximum of sea ice extent) and reaches a minimum at the end of the summer (minimum of sea-ice extent). TMD tends to reduce sea ice coverage during the summer. The amount of incoming shortwave radiation absorbed by the snow layer is higher because the snow albedo switches to its melting value. Therefore snow tends to melt quicker in TMD than BAS and ice starts melting sooner in TMD.

The sea ice volume difference strongly decreased from 1975 to 1981. In 1981 the decrease ends and the difference evolves around an average value of $-2.19 \cdot 10^3 \text{ km}^3$ (1981-1989) and $-1.65 \cdot 10^3 \text{ km}^3$ (1990-1999). This difference of ice volume is explained by thinner ice in regions covered by multi-year ice. Figure 1.5 shows the evolution of the ice thickness difference from 1975 to 2000 in a region covered by multi-year ice.

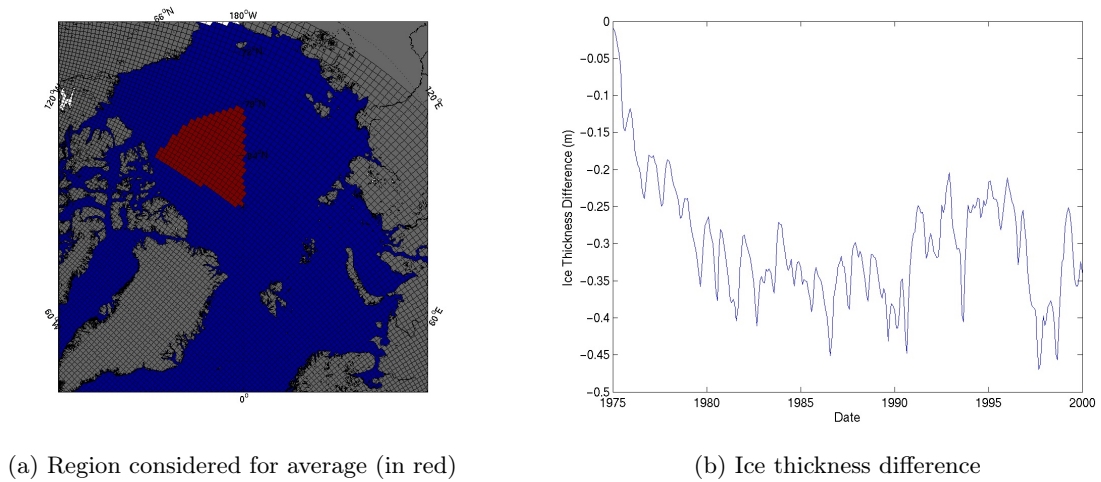


Figure 1.5: Evolution of average ice thickness difference in a region covered by multi-year ice

After the decrease in the difference of average ice thickness a balance seems to be reached in 1981. From 1981 variability is observed around a mean state. The lower snow albedo during the summer still explains the local minimum of ice thickness difference but the lower ice thickness allows higher heat transfer from the ocean to the atmosphere during the winter, increasing sea ice growth. From 1981 the higher sea ice melt during the summer is compensated by a higher growth during the winter. It seems that the insulating effect of the thicker snow cover in TMD does not control winter sea ice growth.

The snow scheme corrections allows for a more realistic behavior of the snow cover and has consequences on sea ice evolution. The ice area is reduced during the summer ($-0.65 \cdot 10^6 \text{ km}^2$ on average) because of the lower albedo of melting snow. The ice thickness in regions covered by multi-year ice decreases. This decrease stops when a balance is established between higher melting in the summer and higher ice growth in the winter due to enhanced heat transfer from the atmosphere to the ocean through thinner ice.

1.4 Comparison with observations

The simulation BAS is an opportunity to compare the results from a long term simulation with data on arctic sea ice derived from satellite remote sensing observations.

Sea ice time series are derived from multi-channel passive microwave data for the period 1978-2004. The Nimbus-7 Scanning Multichannel Microwave Radiometer (SMMR) provided the data from 1978-1987 and the Special Sensor Microwave Imager (SSM/I) has provided data since 1987. Monthly ice concen-

tration for the Northern Hemisphere were produced from the satellite data with the adjusted NORSEX algorithm (Svendsen *et al.*, 1983) and time series of ice area and ice extent were calculated. Those time series have been taken from Johannesssen *et al.* (2002).

The ice extent from observations is compared with the results of the simulation BAS from January 1979 to December 1999 (Figure 2.5). Ice extent is defined as the area with a 15% or higher ice concentration. The sea-ice data from SSMR and SSM/I show a circular section around the North pole which has been never measured due to orbit inclination. The sea ice area and extent in Johannesssen *et al.* (2002) do not include the SMMR pole hole from 1978 to 2002 despite the reduction of the pole hole area across the instrument transition. For the purpose of sea ice extent, we considered that the pixels under the pole hole are always covered by at least 15% of sea ice. The area of the pole hole ($1.38 \cdot 10^6 \text{ km}^2$) is simply added to the ice extent given by Johannesssen *et al.* (2002).

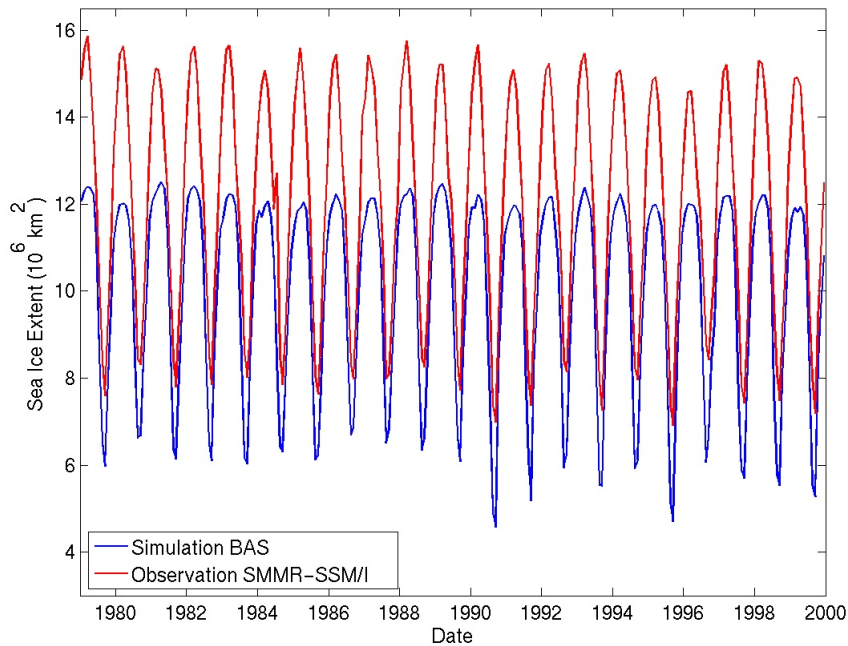


Figure 1.6: Times series of ice extent from satellite observations (red line) and simulation BAS (blue line)

The difference between modeled and observed data during the winter (when ice cover extension is maximal) is partially due to the fact that TOPAZ model does not include Bering sea and Okhotsk sea. However, during the summer, they are free of ice and the observation cover the same area as the model. The minimum sea ice extent can be therefore compared.

Chapter 2

Sea Ice model in NERSC-HYCOM 2.2

2.1 Model Overview

NERSC-HYCOM 2.2 includes two sea-ice models. By default the single-category sea ice model based on *Drange and Simonsen (1996)* is used (referred here as DS96) This model was already implemented in NERSC-HYCOM 2.1. The snow scheme correction (see 1.3) has been implemented in DS96. A multi-category sea ice model referred as ICESTATE has been also coupled to NERSC-HYCOM 2.2.

ICESTATE describes the ice thickness distribution as discrete ice thicknesses, each having an associated coverage. The distribution evolves due to sea-ice dynamics (rafting and ridging) and sea-ice thermodynamics. The sea ice dynamics is described by the Elastic-Viscous-Plastic (EVP) model. The thermodynamics model describes the heat fluxes over water and ice, and also the heat fluxes within the ice and the heat fluxes between the ice and the ocean. A snow cover is included and described as in *Dowville et al. (1995)*. An extended description of the model is given in ????

The ice-ocean model is run in the same configuration used in section 1.1.

2.2 Advection scheme

In response to atmospheric and oceanic forcing the sea ice cover moves. Its dynamics controls the build-up of ice thickness via rafting and ridging, the position of the ice edge and the creation of open-water leads within the ice pack. DS96 and ICESTATE use the EVP model to compute sea-ice velocity. Based on this velocity the horizontal transport of sea ice properties is computed.

Advection in DS96 and ICESTATE In DS96 the ice concentration f , the ice volume $h_i f$ and the snow volume $h_s f$ are advected. In ICESTATE each category is characterized by a fractional area f , an ice thickness h_i , a surface temperature T_s , a brine heat content q_b , a snow depth h_s , a snow albedo α_s and density ρ_s and the temperature of each ice layer (their number depends on the category). The quantities conserved under horizontal transport for each category are the ice area f , the area-weighted surface temperature $f T_s$, the ice and snow volumes $v = f h_{i,s}$, the snow mass $f h_s \rho_s$, the area-weighted snow albedo $f * \alpha_s$, the area-weighted brine heat content $f q_b$ and the heat content of each ice layer $f h_j T_j$.

Numerical scheme Different numerical scheme are available to solve sea ice horizontal transport. *Lipscomb and Hunke (2004)* give the features of an ideal method to transport sea ice :

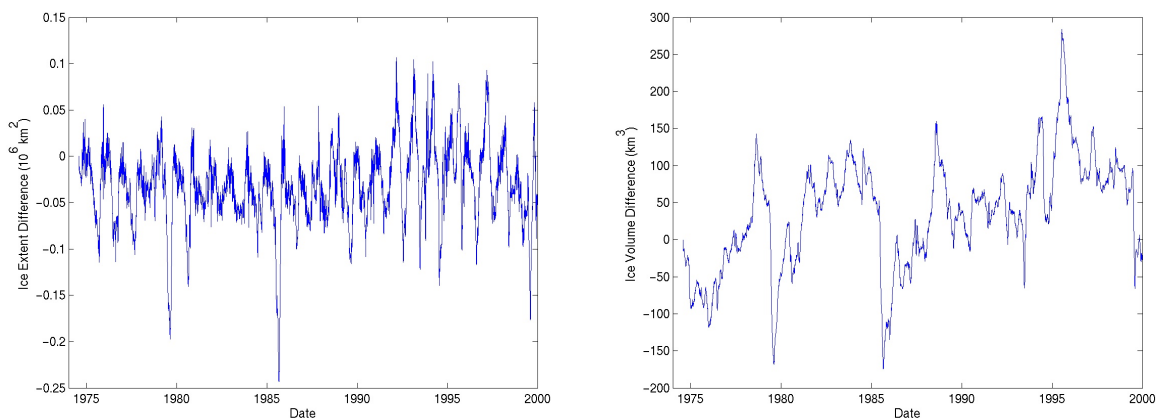
- The method is conservative
- The method is stable.
- The diffusivity is limited by using at a method which is at least second-order accurate in space.

- The method preserves monotonicity of the conserved fields. The method should not create new maxima or minima in conserved quantities.

The Multidimensional Positive-Definite Advection Transport Algorithm (MPDATA, *Smolarkiewicz, 1984; Smolarkiewicz and Clark, 1986*) scheme was used to transport sea ice in DRA96 in NERSC-HYCOM 2.1. MPDATA is conservative, second-order accurate and sign preserving.

Sea ice transport in ICESTATE was first simulated using MPDATA. Unrealistic sea ice accumulations (not shown) were simulated. Instead of MPDATA, the Weighted Essentially Non-Oscillatory (WENO) advection scheme has been tested. WENO has already been implemented in a layered ocean model to transport ocean fields (*Bentsen, personal communication*). *Bentsen* showed that WENO offers a good balance between accuracy and computational cost with small phase and amplitude errors.

Simulations Simulations are performed with DS96 using the two advection schemes. They start in July 74 and last 26 years.



(a) Sea ice area coverage difference WENO-MPDATA

(b) Sea ice volume difference WENO-MPDATA

Figure 2.1: Difference of sea ice cover properties over the Arctic basin between WENO and MPDATA from 1975 to 2000

No significant trend is observed in the difference of sea ice extent and volume between WENO and MPDATA. Over 25 years the average sea ice extent and volume difference are respectively $-30 \cdot 10^3 \text{ km}^2$ and $38,1 \text{ km}^3$.

Since WENO does not change the sea ice properties and pattern compare to MPDATA, we decide to adopt this advection scheme for both models DS96 and ICESTATE. For all the simulations using NERSC-HYCOM 2.2 in the following sections the sea ice transport is computed by WENO.

2.3 Long-term simulation

The sea ice cover evolution from 1974 to 2000 is simulated with DS96 and ICESTATE. ICESTATE is used with 1, 2 and 5 ice categories (table 2.1). The initial ice conditions (concentration, thickness) are the same for all simulations and the meteorological forcing fields are extracted from ERA 40 reanalysis.

The two models simulate different sea ice cover evolution (figure 2.2). The thermodynamics of the models is different (albedo formulation, brine storage and inertial heat flux in ICESTATE) but comparing the results from the simulations enable to highlight processes that explain the observed difference in the sea ice cover.

In wintertime the ice volume is higher in DRA 96 than in ICESTATE with 1 category while the ice volume is similar in summertime (from June to September). ICESTATE with 1 category includes a thermal inertial heat flux to simulate the effect changes of ice heat has on the surface budget and to

N	Upper ice category limits (m)				
1	∞				
2	2.0			∞	
5	0.5	1.0	2.0	5.0	∞

Table 2.1: Upper thickness limit for the different ice categories

keep track of the changes to heat stored in the ice. Without inertial heat flux parametrization, DS96 adjusts immediately to change in the atmospheric heat flux and can simulate higher ice growth during the winter when strong and negative atmospheric heat fluxes are observed. Higher ice melt is also observed with DS96. The albedo formulation used in DS96 does not include snow aging and the albedo for snow switches to its melting value as soon as the surface temperature reaches 0 C. Snow melt is increased and snow disappears earlier. Therefore surface ice melt starts earlier with DS96.

Comparing simulations with ICESTATE for N=1, 2 and 5 categories shows that increasing ice thickness resolution increases ice volume. The annual cycle for ice volume are similar. *Lisæter* (2007) showed that additional ice categories lead to an increased wintertime conductive heat flux through the ice cover and increased ice formation. The enhanced summertime melts of thin ice with more ice categories is not enough to balance the increased wintertime ice formation. An equilibrium thickness is reached for each simulation and the higher is the number of ice categories, the higher is this equilibrium thickness.

DS96 simulates smaller ice extent than ICESTATE. The difference is maximum in summer and exceeds 10^6 km² in September when ice extent is minimum. This difference can be explained by considering the sea ice pattern in Mars and September (figures 2.3 and 2.4).

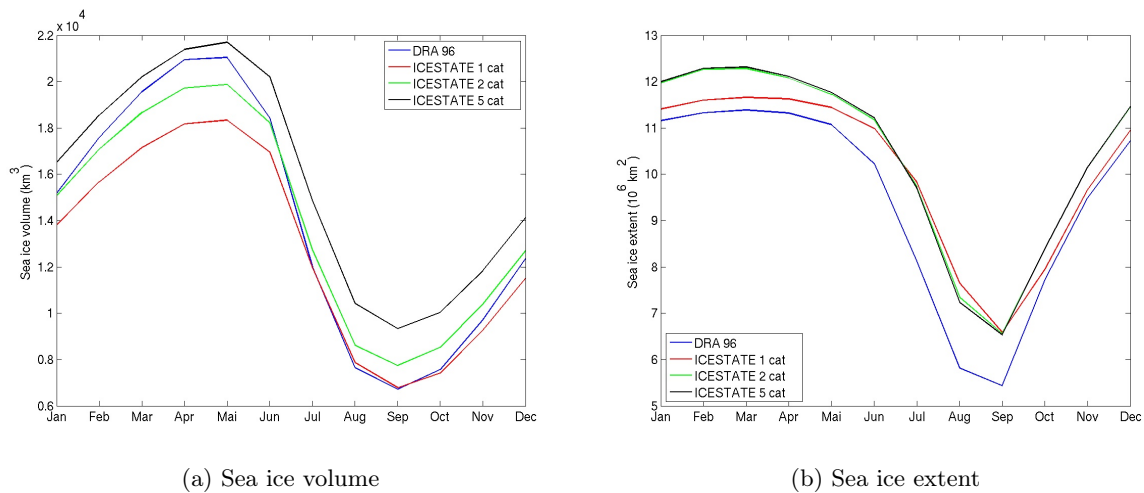


Figure 2.2: Average evolution of sea ice cover properties over the Arctic basin (1975-2000)

In winter maximum ice thickness is simulated north from Greenland and from the Canadian Archipelago. In Central Arctic and in the Beaufort sea ice thickness is larger with DS96 than with ICESTATE (except for N=5 ice categories). On the other hand DS96 simulates smaller ice thickness in the peripheral regions (Baffin Bay, Fram Strait, Kara Sea).

The summertime (September) ice pattern shows maximum north of Greenland and north of Queen Elizabeth Islands for all the simulations. As noticed previously DS96 shows a smaller ice extent than ICESTATE. Main differences are observed in the Laptev Sea and the Kara Sea. Those regions are the same as the regions where DS96 simulates thinner ice during the winter.

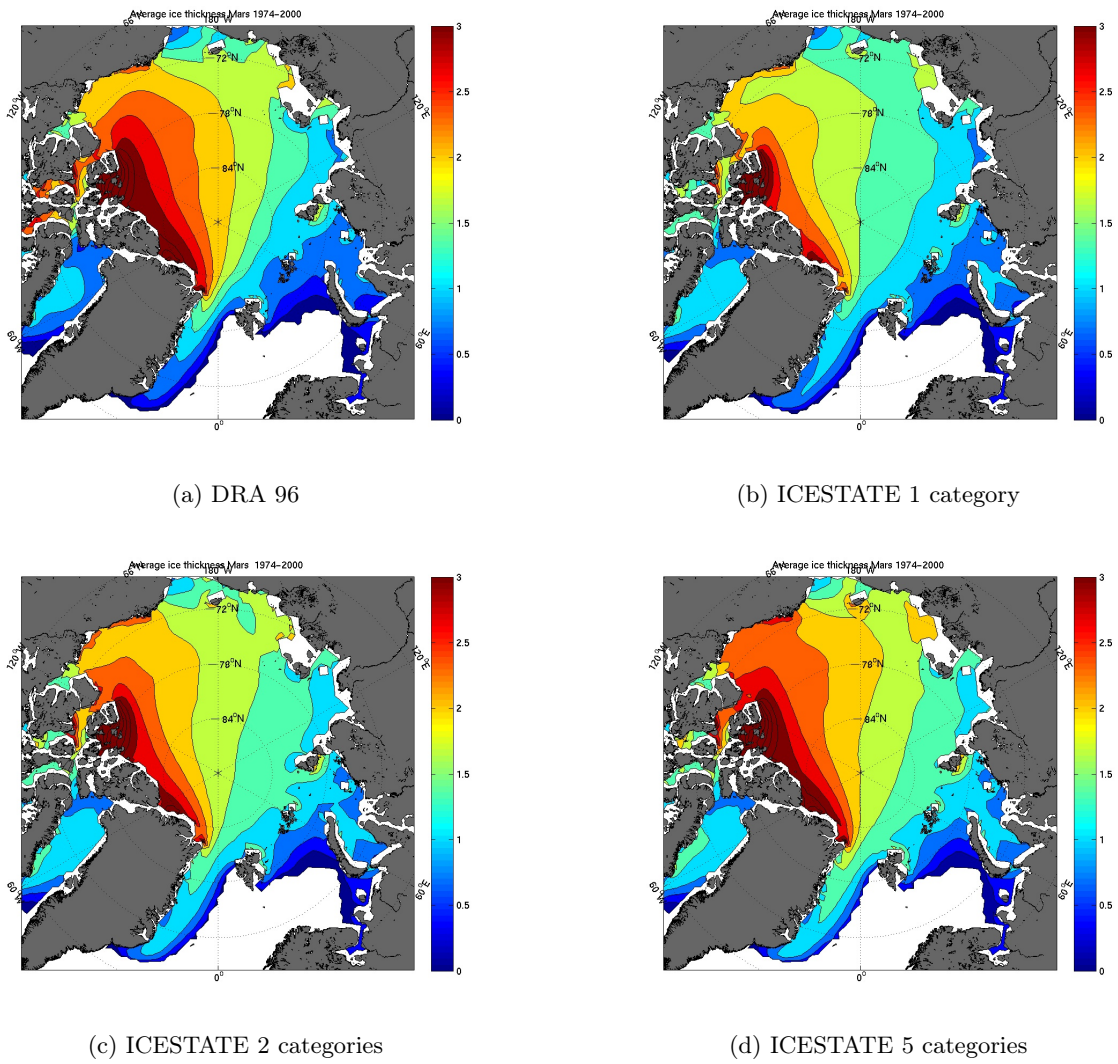


Figure 2.3: Average ice thickness (1975-2000) in Mars over the Arctic Ocean for 4 simulations (DS96, ICESTATE with $N = 1, 2$ and 5 ice categories). The ice thickness is shown for grid cells with an ice concentration higher than 0.15

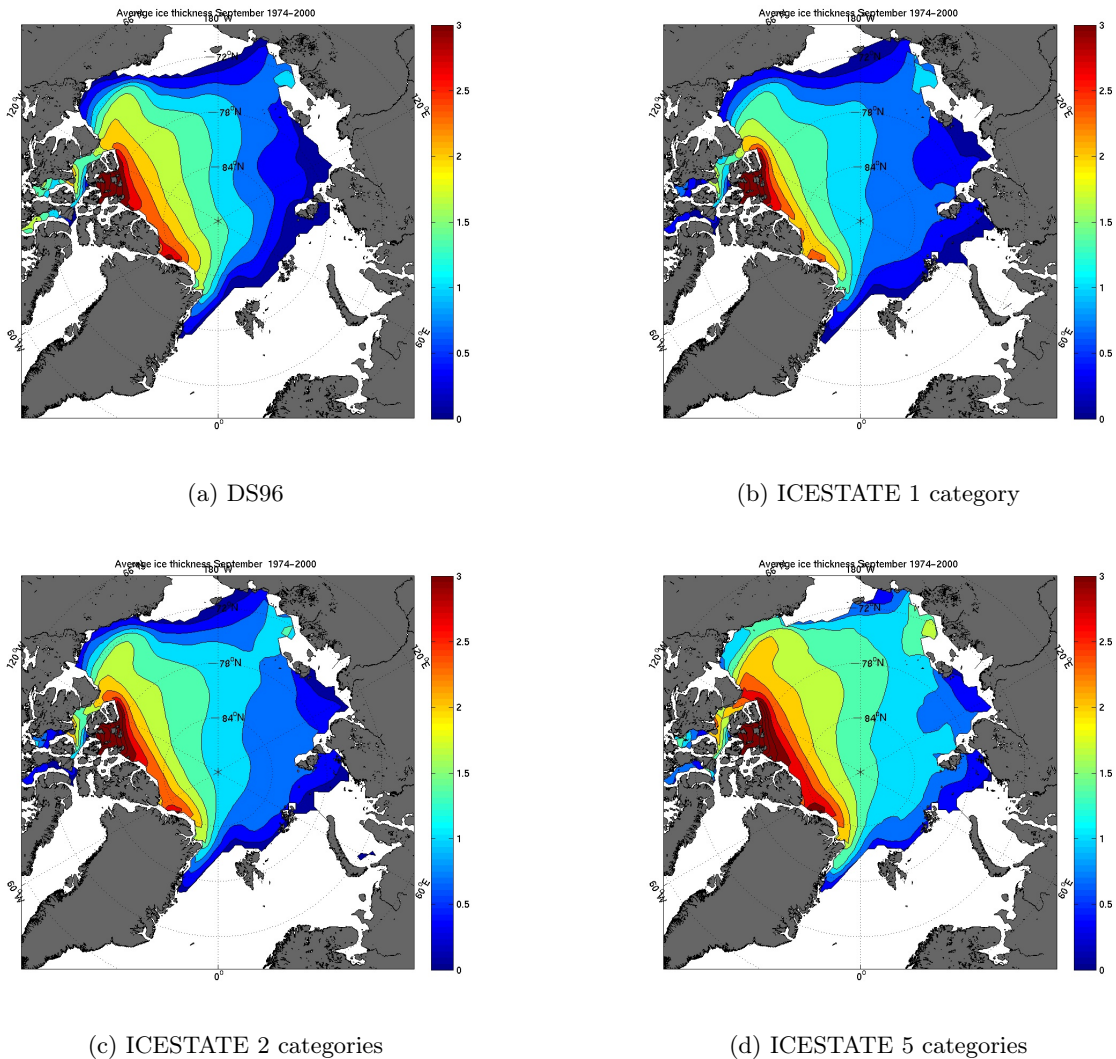


Figure 2.4: Average ice thickness (1974-2000) in September over the Arctic Ocean for 4 simulations (DS96, ICESTATE with $N = 1, 2$ and 5 ice categories). The ice thickness is shown for grid cells with an ice concentration higher than 0.15

Comparison with observations The simulated ice extent can be compared with satellite observations from 1979 to 2000 (figure 2.5). The observations are the same as those used in 1.4.

The difference between modeled and observed data during the winter (when ice cover extension is maximal) is partially due to the fact that the grid used in the experiments does not include Bering sea and Okhotsk sea. However, during the summer, they are free of ice and the observations cover the same area as the model. The minimum sea ice extent can be therefore compared.

As observed in section 1.4, DS96 underestimates the summer ice extent. Figure 2.6 shows that sea ice simulated with DRA 96 in September is less extended compared to observations in the Kara Sea, the Fram Strait and at the North of Alaska.

The evolution of the ice extent in summer (July, August and September) is the same for ICESTATE whatever the number of categories. The simulated ice extent with ICESTATE is lower than the observed ice extent during the summer. Compared to observations, ICESTATE underestimates the ice extent in the Fram Strait and at the north of Alaska (figure 2.6). Besides it tends to simulate too much ice in the Laptev Sea.

The difference with observations at the North of Alaska may be explained by the fact that the Bering Strait is a model boundary. The model is set up with a 0.8 Sv barotropic transport into the Arctic from the Bering Strait. However *Woodgate et al.* (2005) showed that the Bering Strait flow has strong seasonal

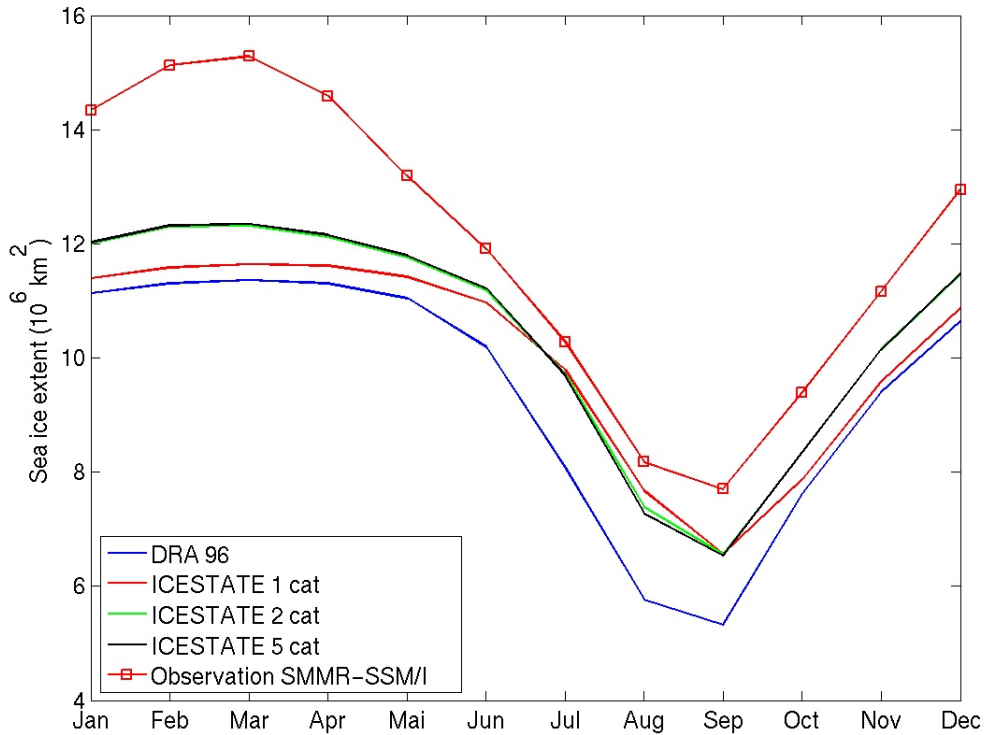


Figure 2.5: Average ice extent for the period 1979-2000 for 4 simulations (DS96, ICESTATE with N = 1, 2 and 5 ice categories) compared to satellite observations

variability, resulting in large variations in waters supplied to the Arctic. Using the monthly climatology of *Woodgate et al. (2005)* may improve the quality of the simulations in the Chukchi sea. The difference observed in the Fram Strait may be due a incorrect simulation of the ocean circulation in the Greenland Sea. This must be more deeply investigated.

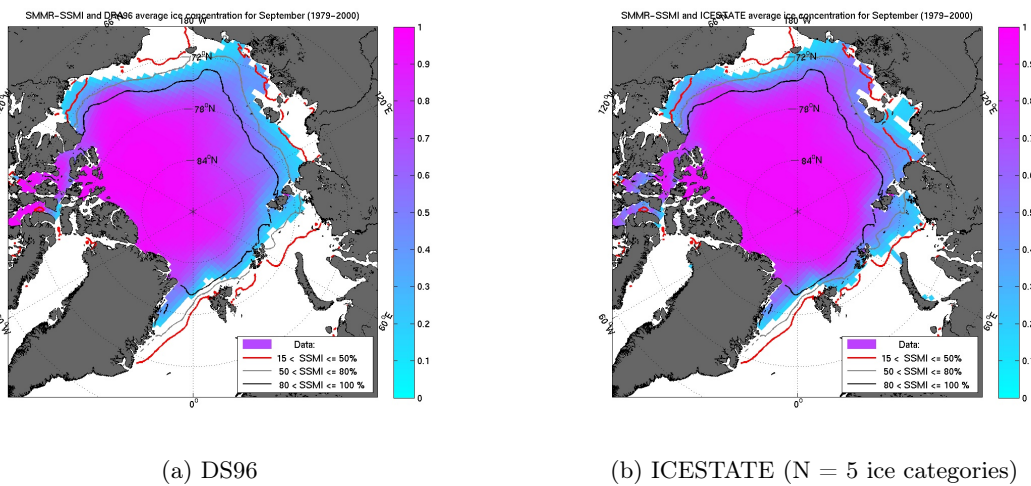


Figure 2.6: Simulated ice concentration (>0.15) in September for the period 1979-2000 compared to observations from SMMR-SSM/I. Red line indicates the position of the ice edge (ice concentration higher than 0.15) based on observations.

Chapter 3

Albedo evolution

The determination of sea ice albedo in models is essential for proper treatment of the ice-albedo feedback. Increased surface temperature may cause a reduction in the area covered by snow/ice, which would in turn increase absorption of solar radiation in the Arctic Ocean and a further increase in surface temperature. A correct estimation of sea-ice albedo is necessary to reproduce satisfyingly the growth and melt of sea ice and its snow cover.

The albedo simulated in TOPAZ is compared with observed summer albedo over the period 1982-1998 (*Laine*, 2004). The need for an adjustment of sea-ice albedo is identified.

Many snow/sea-ice albedo parameterizations have been developed but few data are available to validate those parameterizations. Among those data, the observation from the SHEBA experiment (Surface Heat Budget of the Arctic Ocean) are certainly the highest quality suite of surface properties ever made in the Arctic Ocean. The quality of the albedo scheme used in the sea-ice component of TOPAZ is assessed by comparison with albedo observations from SHEBA and results from other albedo parameterizations. Improvements are suggested and we pay a particular attention to the effect of melt ponds on area-average albedo.

3.1 Albedo: comparison with observations

3.1.1 Data

Laine (2004) used the advanced very high resolution radiometer (AVHRR) Polar Pathfinder data to compute a summer albedo data set over the Arctic from 1982 to 1998. Narrow-band satellite observations are converted to broad-band surface albedo measurement with corrections for cloud cover, atmospheric attenuation and sun angle. These observations are estimated to have errors of 5-10% (*Xiong et al.*, 2002). In this study the sea ice albedo is referred as the albedo of the sea ice region and therefore includes the component from leads. Sea ice regions are regions having an ice concentration between 10% and 100%. Cloud detection and identification of cloud-free pixels is a critical point in measuring the surface albedo. Indeed contamination of cloud pixels could result in an overestimate of albedo. *Laine* (2004) identified this limitation. The summer albedo dataset contains only clear sky albedo estimations that does not represent the actual albedo in all meteorological conditions. Under cloudy conditions the spectral distribution of the incoming shortwave radiation is different.

3.1.2 Albedo comparison

The simulated surface albedo is extracted from the 25-year simulation BAS and TMD (see 1.3.3) and compared to the summer albedo dataset from *Laine* (2004).

An example: 1984 The summer albedo (figure 3.1) in 1984 is representative of the Arctic albedo between 1982 and 1998. June shows the higher albedo with sea ice still partially covered by snow with

high reflectivity. The observations show lower albedo than the simulation in the Beaufort, Chukchi and Kara Seas and in the Canadian Archipelago. In July the model simulates a uniform albedo (around 0.55) in area largely covered by ice (ice concentration higher than 0.95). The observations show a less uniform pattern with an albedo maximum in the central Arctic (latitude > 84N). Both monthly simulated and observed albedo increase in August due to the first snowfall in late August.

Global evolution The sea ice albedo for the whole Arctic (including Hudson Bay) has been calculated for each month from 1982 to 1998 (figure 3.2). For the simulation BAS, figure 3.2 (a) shows that the model simulates higher albedo than the observations of *Laine* (2004). The observed and simulated albedo are minimum in July.

The evolutions in TMD lead to an albedo closer to the observations (figure 3.2 (b) and table 3.1). The snow albedo is allowed to decrease to its melting value and therefore reduced the global albedo in June (0.54 for TMD and 0.59 for BAS).

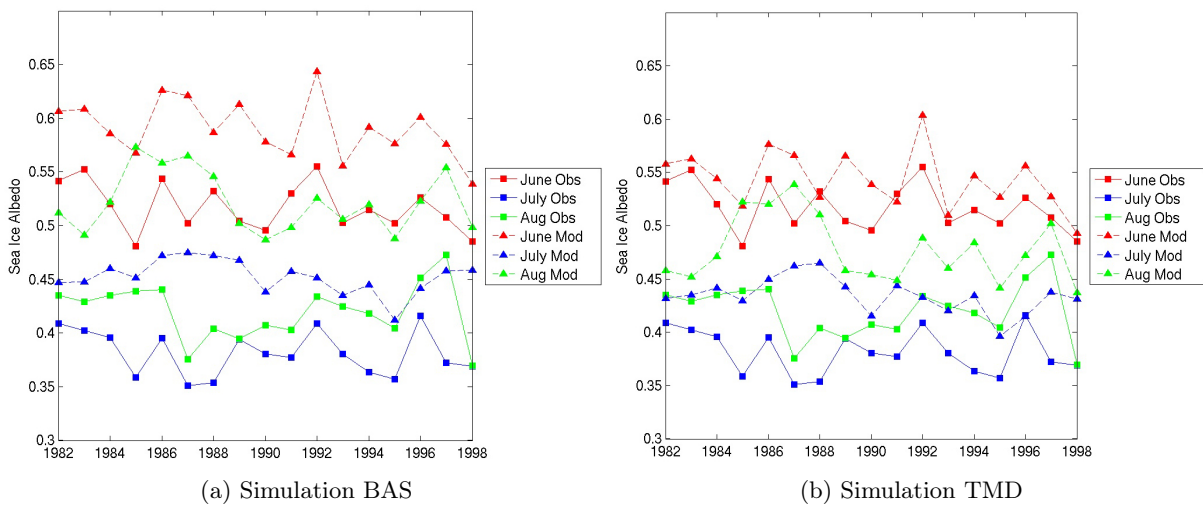


Figure 3.2: Monthly averaged Arctic sea ice albedo from 1982 to 1998

	June	July	August
Observations	0.52	0.38	0.42
BAS	0.59	0.45	0.52
TMD	0.54	0.43	0.48

Table 3.1: Monthly averaged Arctic albedo

Laine (2004) showed that the summer albedo is correlated with ice concentration in the fringe areas. Indeed, due to the low albedo of ocean water (around 0.06), lead formation causes a strong decrease of the surface albedo. But in the central part of the Arctic Ocean where the sea ice concentration is very high even during the summer (*Laine*, 2004), the ice concentration does not play a very important role in total surface albedo. The albedo evolution depends on ice surface features change such as snow cover or melt ponds development.

The albedo in the central Arctic is higher than for the global Arctic (figure 3.3 and table 3.2) due to the quasi-absence of leads. The simulated albedo is still higher than the observed albedo for the 3 months. The snow albedo correction in TMD allows for a better agreement with observations, especially in June. Despite this modification the gap between observed and simulated albedo is still consequent in

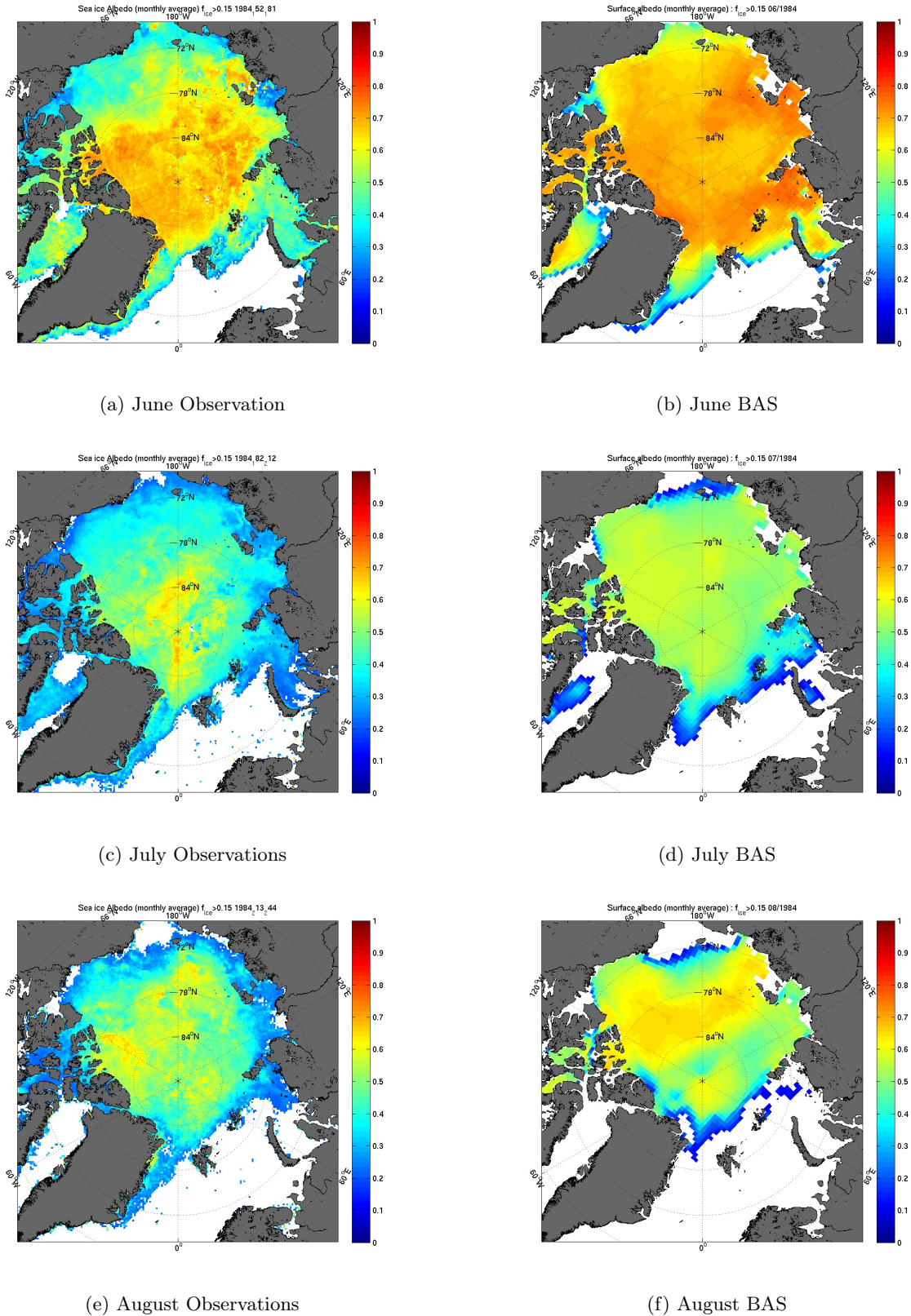


Figure 3.1: Albedo over the Arctic in 1984; Left: Observations; Right: Model

July and August when most of the ice is snow-free. This difference may arise because the sea-ice albedo parameterization in TOPAZ does not include melt-pond which decreases strongly the surface albedo. Melt ponds development is not only observed on coastal sea ice (*Grenfell and Perovich, 2004*) but also in the central Arctic. *Perovich et al. (2008)* observed in early September 2005 melt ponds fractions up to

0.2 at latitude higher than 85N.

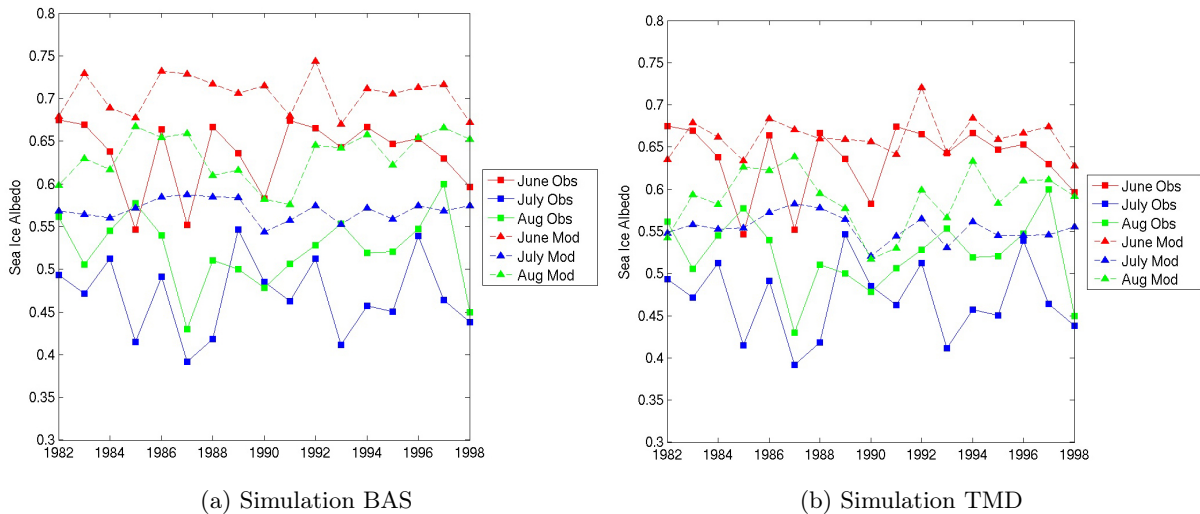


Figure 3.3: Monthly averaged sea ice albedo from 1982 to 1998 in the central Arctic (region considered is shown figure 1.5)

	June	July	August
Observations	0.64	0.47	0.52
BAS	0.71	0.57	0.63
TMD	0.66	0.55	0.59

Table 3.2: Monthly averaged albedo in the central Arctic (region considered is shown figure 1.5)

The simulated summer albedo over the Arctic shows higher values than the observations. To test with more accuracy the snow/sea ice albedo scheme implemented in TOPAZ, the data from the SHEBA campaign are used.

3.2 Albedo evolution from SHEBA

3.2.1 Observational data

The SHEBA experiment included a one-year long (2 October 1997 to 11 October 1998) field program centered on a drifting ice station in the Beaufort Sea. Measurements of surface temperature T_s , atmospheric temperature at 10m T_a , precipitations, snow depth, ice thickness and surface albedo are obtained from the SHEBA atmospheric surface flux group (Persson *et al.*, 2002) and Snow and Ice Studies CD-ROM (Perovich *et al.*, 1999) were used.

The atmospheric forcing were registered each hour at the tower. Precipitation are considered as snow when both T_s and T_a are below 0 C.

Ice thickness was measured at a 50-m line using gauges spaced every 2.5 or 5 m named as the Mainline for mass balance. Data are available weekly from October 1997 to May 1998 and in September 1998 and every 1-2 days from June to August. Even if the snow depth h_s was measured every 1-5 m along a 500 m-long line, we decided to use the snow depth measured along the Mainline for mass balance

to get consistent dataset. The spatially averaged snow depth and ice thickness has been computed for each day (by linear interpolation for days without measurements). Their evolution is shown figure 3.4.

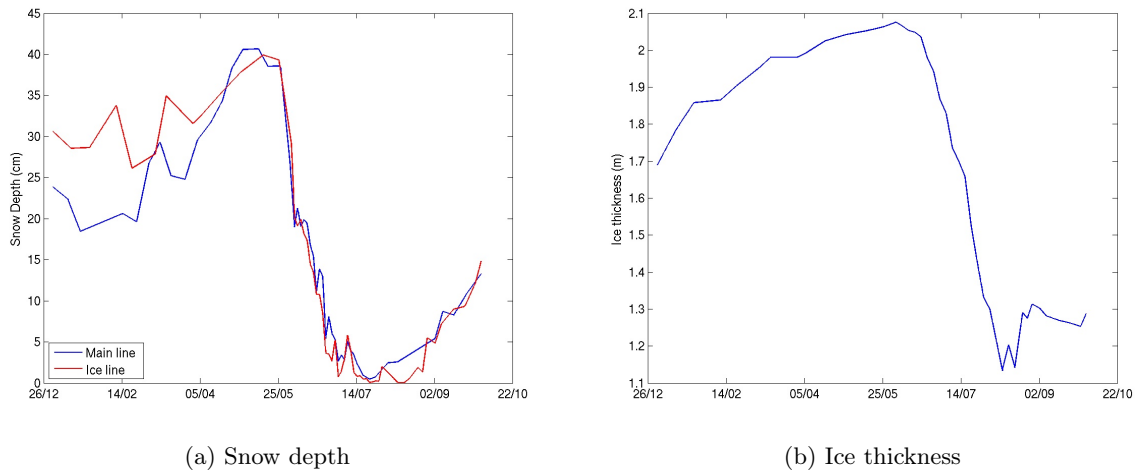


Figure 3.4: Daily averaged SHEBA observed snow depth and ice thickness from 01 January 1998 to 28 September 1998

Albedo measurements were made at every 2.5 m along a 200 m-long line that encompassed different snow and ice conditions over multi-year ice. The values were then averaged for each day to get an estimation of an area average albedo. Figure 3.5 shows the albedo temporal evolution. *Perovich et al.* (2002a) divided the albedo time series into five sections that denote the distinct phases of the seasonal evolution of albedo: dry snow, melting snow, pond formation, pond evolution and fall freeze-up.

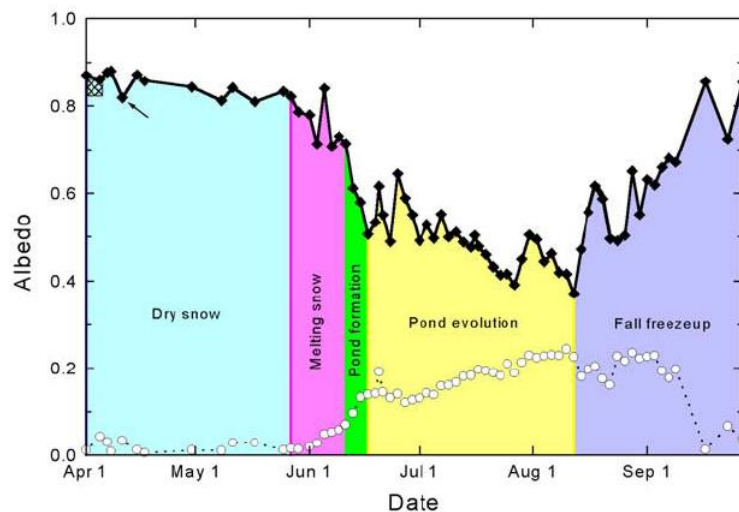


Figure 3.5: Time series of wavelength-integrated albedo from *Perovich et al.* (2002a). The standard deviation of albedo measured along the albedo line is plotted as open circle

3.2.2 Description of albedo parameterizations

The first parameterization is described in *Drange and Simonsen* (1996) and referred as DS96. This is the albedo scheme uses currently in TOPAZ. The snow albedo is given by equation 1.1. In DS96 the albedo of ice depends on whether the surface is at the melting point or below. If it is at the melting point, the

albedo is set to the value $\alpha_{i,m}$ (0.50), whereas if the surface is dry it is set to $\alpha_{i,d}$. If the ice surface is dry and snow-free, the thin ice albedo parameterization of *Maykut* (1982) is used. The albedo depends on the ice thickness h_i according to:

$$\alpha_{i,d} = \min(0.73, 0.08 + 0.44h_i^{0.28}) \quad (3.1)$$

DS96 assumes that the surface albedo is equal to the snow albedo when snow is present on the ground ($h_s > 0$).

In most climate models the surface albedo on land is a weighted value between the snow and bare ground albedo. A snow cover fraction is computed based on snow depth (for a review of different snow cover fraction in climate models see *Pedersen and Winther* (2005)). The snow cover fraction increases with snow depth and reaches 1.0 for deep snow depth in most of the models. Several sea ice models include a fractional snow covered area (e.g. *Hunke and Lipscomb* 2008) to account for non-uniform snow distribution within a grid cell. The Los Alamos sea ice model (CICE) weighted the ice and snow albedo according to:

$$f_{snow} = \frac{h_s}{h_s + h_{snowpatch}} \quad (3.2)$$

and $h_{snowpatch} = 0.02$ m. We combine this snow cover fraction with the snow and ice albedo given by DS96 to get an area average albedo. It is referred as DS96-SC.

Snow optical properties depends on grain size and shape, depth of the snow layer, optical properties of the underlying surface, surface roughness, liquid water content and any impurities. The sea-ice model developed by *Salas-Méllia* (2002) included a more advanced treatment of snow albedo than DS96 and includes snow aging processes following *Douville et al.* (1995). The snow albedo is allowed to vary between $\alpha_{s,min}=0.5$ and $\alpha_{s,max}=0.85$. After a snow fall the albedo is increased:

$$\alpha_s(t + \Delta t) = \alpha_s(t) - \Delta t (\alpha_s(t) - \alpha_{s,max}) \frac{P^s}{P_{s,new}^s} \quad (3.3)$$

where $\alpha_s(t)$ is the snow albedo at a given time t , P^s is the equivalent liquid precipitation (m/s) and $P_{s,new}^s = 0.002$ m the amount of snow in equivalent liquid precipitation that is necessary to refresh the snow surface albedo to its maximum value. When no snow falls, the snow albedo decreases with time. For melting and rainy, and dry cold conditions the decaying formulas are:

$$\alpha_s(t + \Delta t) = \begin{cases} \alpha_s(t) - \frac{\tau^a}{\tau^1} \Delta t & \text{when } T_{surf} < 0 \text{ C} \\ (\alpha_s(t) - \alpha_{s,min}) \exp\left(\tau^f \frac{\Delta t}{\tau^1}\right) + \alpha_{s,min} & \text{when } T_{surf} = 0 \text{ C} \end{cases} \quad (3.4)$$

where τ^a, τ^f and τ^1 are 0.008, 0.24 and 86400 s respectively.

This parameterization is combined with the snow cover fraction from CICE and the ice albedo calculated as in DS96 to get an area-average albedo and is referred as SAM02.

3.2.3 Albedo evolution

The seasonal cycle of surface albedo over sea ice is determined using the above parameterizations and the data described in 3.2.1 (figure 3.6). Surface albedo from the albedo line are used in comparison. The albedo calculated in the SHEBA conditions is representative of what each parameterization would calculate in a grid covered by sea ice. The influence of leads on the grid-cell sea ice albedo is not included.

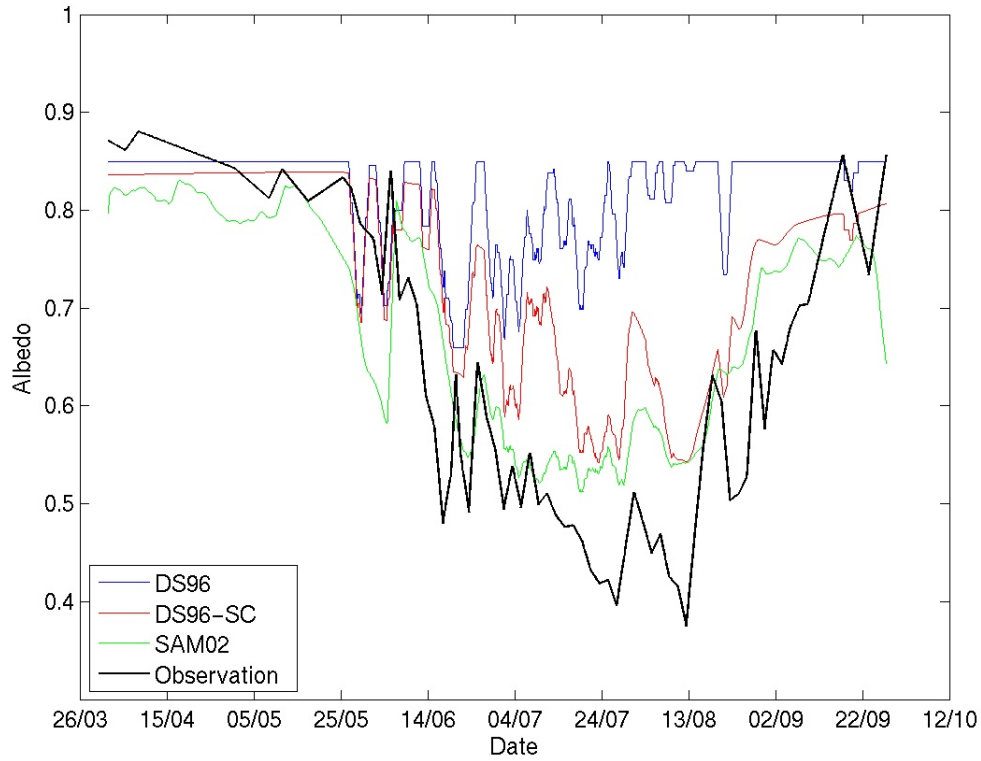


Figure 3.6: Comparison of parameterized albedo versus observed surface albedo. Solid black line represents the observed albedo and colored lines the parameterized albedos.

The albedo for DS96 remains constant before the melting period. When the melting period starts (on May 27), the albedo decreases to the value for melting snow ($\alpha_{s,melt} = 0.66$). Since the surface temperature oscillates between negative and positive temperature and the snow is still present in the grid cell (even at really small depth), the surface albedo in DS96 oscillates between the value for dry and melting snow. When the temperature crosses the threshold value, unrealistic step changes are observed in snow albedo. The situation may be different in a sea-ice model where temperature variations are much smoother than in SHEBA where 1-hour averages were used as input in the albedo parameterization.

The introduction of a snow cover fraction (DS96-SC) leads to a better reproduction of the season cycle of surface albedo. The albedo decrease during the pond evolution period due to the decrease of f_{snow} but the area-average albedo is still overestimated. This formulation does not include melt ponds formation and development that reduce the area average albedo during the summer.

SAM02 aims at reproducing the effect of snow aging process. During the winter the rate of decrease of snow albedo is correctly reproduced but a bias remains that may arise from an underestimation of dry snow albedo. At the beginning of the melt season (on May 27) a strong decrease is observed in the area-average albedo. SAM02 underestimates the total albedo due to its low value for the albedo of melting snow. The steady decline in albedo as the melt ponds grew deeper and larger in areal extent is not reproduced even if SAM-02 simulates the lower summer albedo among the parameterizations compared in this study.

DS96 fails to predict correctly seasonal albedo evolution during SHEBA. The results are improved with DS96-SC when a snow cover fraction is used to combine snow and ice albedo. *Liu et al.* (2007) determined that snow depth plays a more important role than surface temperature or ice thickness in determining the albedo using the SHEBA measurements. Introducing snow aging processes (SAM02) allows

for a more realistic evolution of dry snow albedo and avoids unrealistic drops in snow albedo observed with temperature dependent scheme such as DS-96 when temperature reaches a threshold value. However none of the albedo parametrization used in this study are able to reproduce low albedo value observed during the ponds formation and evolution periods. They does not include an explicit representation of melt ponds.

3.3 Melt ponds evolution

3.3.1 Observations during SHEBA

Melt ponds substantially reduce the surface albedo during the summer and increase the amount of incoming shortwave radiation absorbed by the sea-ice cover. The albedo of ponded ice ranges typically from 0,2 to 0,4 and depends on melt ponds depth and underlying ice optical properties (*Morassutti and LeDrew, 1996*). Melt ponds mostly cover between 10% and 50% of the ice surface (*Fetterer and Untersteiner, 1998*). The melt pond fraction depends on surface roughness, snow cover, ice type as illustrated by *Eicken et al. (2004)*.

During SHEBA the melt ponds fraction reaches 40% in early August along the 200m albedo-line with a maximum average depth of 40 cm (figure 3.7). Maximum pond fraction of the general SHEBA area determined from aerial photographs was 24% (*Perovich et al., 2002b*). Despite a larger pond fraction for the albedo line, the surface-based and aerial observations exhibited the same temporal dependence (*Perovich et al., 2002a*). The pond fraction decreased first as the ice became permeable and ponds drained.

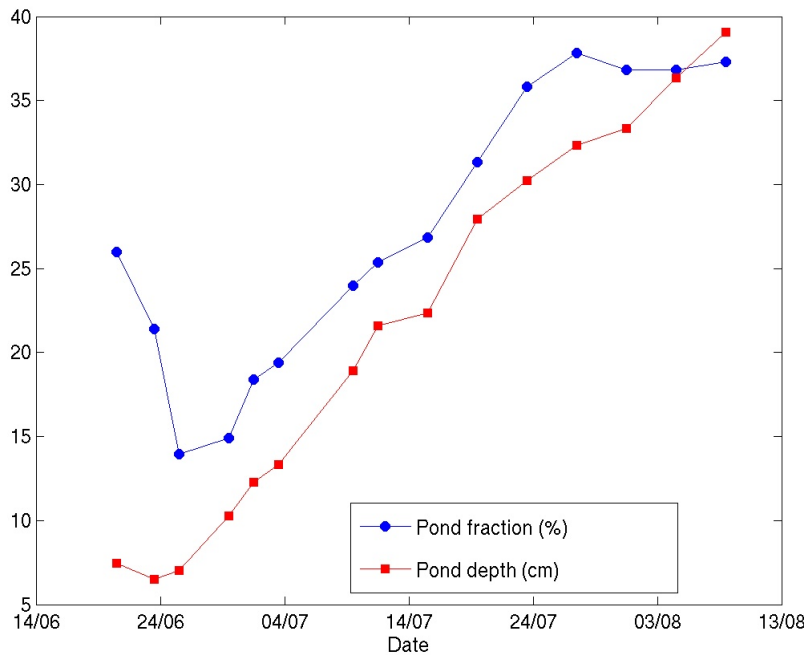


Figure 3.7: Evolution of melt ponds during SHEBA: time series of the pond fraction and depth measured along a 200-m-long line

3.3.2 Ponds evolution modeling

Mathematical models have been developed to simulate melt ponds evolution and have improved the understanding of the processes governing melt pond evolution (*Taylor and Feltham, 2004; Lüthje et al.,*

2006). Because of their complexity they are not suitable for inclusion in the sea ice model used in TOPAZ. *Koltzow* (2007) used the observations from the SHEBA project to include the effects of melt ponds on the summer albedo. Melt pond fraction f_p is approximated by the surface temperature T_s (C):

$$f_p = 0.11(2 + T_s) \quad T_s \geq -2^\circ\text{C} \quad (3.5)$$

No melt ponds are observed for temperature below -2C. In *Koltzow* (2007) the albedo scheme including this melt pond parametrization has lower systematic error than other schemes regarding absorbed solar radiation. However this approximation assumes pond formation as soon as snow starts melting and predict a too low albedo in early summer (*Koltzow*, 2007). *Enomoto* (2007) found that this melt pond parametrization introduces fluctuation at the day-to-day scale and does not reproduce well the albedo seasonal evolution.

The Los Alamos sea ice model (*Hunke and Lipscomb*, 2008) includes a new melt ponds parametrization (referred here as BA08) that simulates melt water accumulation and ponds development. The melt ponds volume v_p (defined as the products of pond area, f_p , and average depth h_p) grows through addition of ice or snow melt water or rain water and shrinks when the ice surface becomes cold:

$$\text{pond growth: } v'_p = v_p(t) + r_1 \left(dh_i \frac{\rho_i}{\rho_w} + dh_s \frac{\rho_s}{\rho_w} + P_{rain} \Delta t \right) \quad (3.6)$$

$$\text{pond contraction: } v_p(t + \Delta t) = v'_p \exp \left[r_2 \frac{\max(T_p - T_s, 0)}{T_p} \right] \quad (3.7)$$

where dh_i and dh_s represent ice and snow surface melt during Δt , $r_1 = 0.1$ specifies the fraction of available liquid water captured by the ponds and $r_2 = 0.01$. T_p is a reference temperature equals to -2C and P_{rain} the equivalent liquid precipitation (m/s). Pond depth is assumed to be a linear function of pond fraction ($h_p = 0.8f_p$).

3.3.3 Comparison with observations

The melt ponds evolution depends on the quantity of melt water available. We use the data concerning melt ponds from Sheba and compare them with results from simulation with BA08.

Ice and snow melt rates are calculated from the time series of ice thickness and snow depth along the Mainline for mass balance. The melt rate f is computed as in *Perovich et al.* (2003):

$$f = \frac{H_{i,s}(t_{j+1}) - H_{i,s}(t_j)}{t_{j+1} - t_j} \quad (3.8)$$

where $H_{i,s}$ is the ice/snow thickness, t_j is the time of one measurement and t_{j+1} is time of the next measurement.

The melt rates are applied at a 1-hour time step consistent with the meteorological data described in 3.2.1. To compute melt pond volume snow and ice density are respectively set to 400 and 900 kg/m⁻³. The melt ponds volume simulated with BA08 is compared with observations from SHEBA during the summer 1998 (figure 3.8).

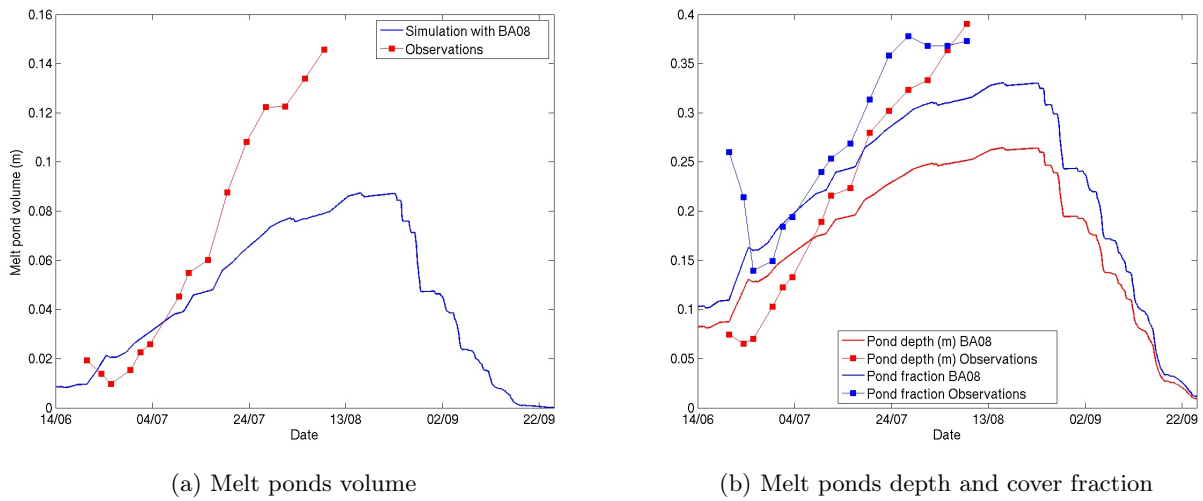


Figure 3.8: Time series of melt ponds properties at SHEBA. Comparisons with observations

Melt ponds volume simulated with BA08 is in correct range compared to the observations. However volumes simulated in the second part of the summer (from mid-July) are lower than the observations. The simulated pond fraction and depth increased during the summer but do not reach the maximum values observed in early August. The linear relationship between pond depth and fraction does not allow to reproduce all the complexity of the ponds evolution such as the shrinkage of melt ponds due to drainage in late June. In BA08 pond fraction and depth starts decreasing when temperature is lower than T_p . The fall freeze-up (in BA08) with a formation of ice skims on the surface of ponds and the reduction of pond fraction started on 25 August. Airborne measurements (*Tschudi et al.*, 2001) showed than pond fraction over an area of several km^2 around SHEBA site reached 0 between 27 August and 13 September while simulated pond fraction in BA08 is still equals to 0.15 on 8 September. The quick reduction of pond fraction at the end of the summer is not reproduced in BA08.

3.3.4 Adaptation of melt ponds parameterization

Based on the observations made in 3.3.3 the melt ponds parametrization is adapted. Melt pond volume accumulation and shrinkage are adjusted.

BA08 assumes that 10% of the available liquid water is captured by the ponds. *Ebert and Curry* (1993) fixed to 15% the fraction of surface meltwater that accumulates at the surface in melt ponds. They highlight that this quantity is highly uncertain. Based on the observation from SHEBA we decide to adopt $r_1=0.16$.

The pond volume shrinks when the ice surface become cold. At a given temperature the reduction of pond volume depends on the constant r_2 . To get a better reproduction of ponds shrinkage we take $r_2=0.03$.

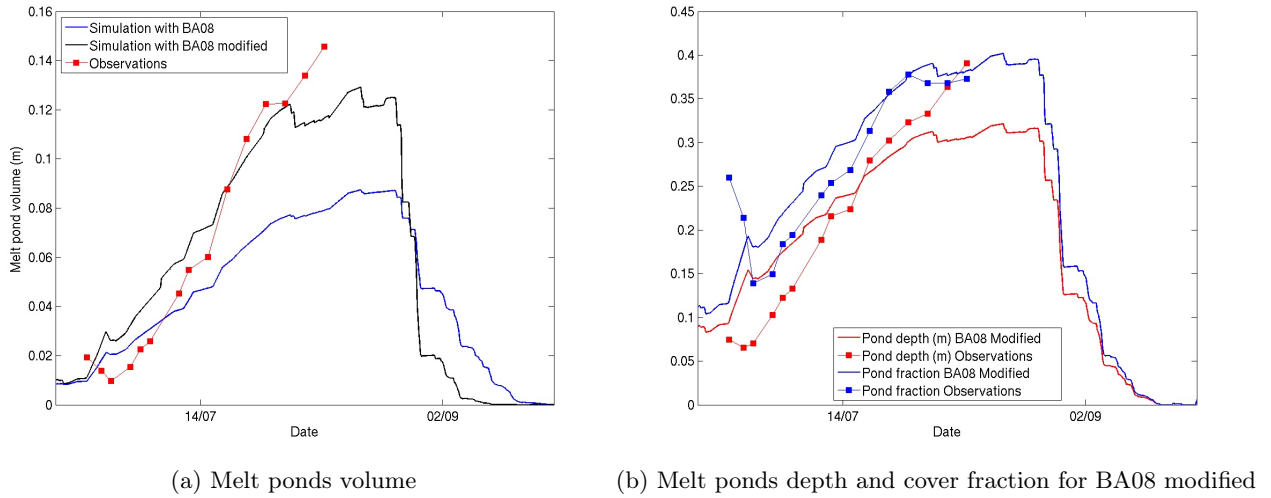


Figure 3.9: Comparisons of melt pond properties with observation: effects of BA08 modification

The increase of pond volume (Figure 3.9 (a)) during the summer is better reproduced with BA08 modified. The shrinkage of melt pond volume is faster in BA08 modified than in BA08 which is in a better agreement with the observations of *Tschudi et al.* (2001). The melt ponds fraction reaches a maximum value of 0.4 against 0.37 in the observations. The maximum melt pond depth (0.40 m) in early August is not reproduced due to the linear relationship between melt ponds depth and fraction.

We decide to keep the relationship used in BA08 ($h_p = 0.8f_p$) even if this relation does not make any distinction between first-year ice (FYI) and multi-year ice (MYI). Indeed the spatial distribution of melt ponds depends on the topography of snow and sea ice. On FYI (smoother than MIY), melt ponds are less deep but cover a larger area (*Eicken et al.*, 2004). On the contrary on rougher MYI melt ponds formed in depressions are deeper but cover a smaller area.

3.4 Final albedo formulation

As shown before, the albedo scheme used in TOPAZ fails to reproduce albedo seasonal evolution. Based on the observations made in 3.2.3 and on the melt pond parameterization described in 3.3.4 a new snow/sea ice albedo is proposed.

3.4.1 Formulation

The snow/sea ice albedo scheme SAM02 produced the best results when simulated albedo is compared to observations for SHEBA. The snow albedo scheme used in SAM02 has been compared to albedo observations in other place in the Arctic: Ny-Alesund (Svalbard, *Pedersen and Winther* (2005)) and Barrow (Alaska, *Mölders et al.* (2008)). This parameterization performs well as long as numerous snow events reset the snow albedo to its maximum value. In low precipitation sites such as Barrow and Ny-Alesund, *Pedersen and Winther* (2005) and *Mölders et al.* (2008) showed that the parametrization underestimates the snow albedo during months with only few snow events. *Pedersen and Winther* (2005) explained that the snow albedo is too rarely reset to its maximum value due to a large precipitation threshold (10 mm SWE in *Douville et al.* (1995)). SAM-02 used a lower precipitation threshold (2 mm SWE) so that the albedo is more easily reset to its maximum value. In dry snow conditions, during the SHEBA experiments, the rate of decrease of the snow albedo is satisfyingly reproduced in SAM-02.

During the melt season, a prognostic scheme such as SAM-02 avoids unrealistic drops in snow albedo observed with temperature dependent scheme such as DS-96. *Mölders et al.* (2008) identified that prognostic albedo scheme performs best in the melting season. We decide to keep this snow albedo scheme. To avoid the strong decrease of snow albedo at the beginning of the melt season (29 Mai), the value of melting snow albedo is set to 0.72.

The melt pond parameterization described in 3.3 is coupled with SAM02. The melt pond albedo depends on melt pond depth. It is based on the *Ebert and Curry* (1993) albedo parameterization with an improved pond parameterization as reported in *Schramm et al.* (1997). The improvements are based on the pond albedo observation in the Canadian Arctic Archipelago reported by *Morassutti and LeDrew* (1996). We use the melt ponds albedo for MYI reported in *Schramm et al.* (1997). The albedo is divided in four spectral bands (0.25-0.69, 0.69-1.19, 1.19-2.38, and 2.38-4.00 μm). To get a broadband albedo the four bands are averaged with appropriate spectral weighting as in *Lindsay* (2003). For clear skies the weights are 0.500, 0.346, 0.144, and 0.010 and for cloudy skies they are 0.582, 0.343, 0.074, and 0.0002. The difference of broadband albedo between clear and cloudy skies is low so that we use the arithmetic average to get the melt pond albedo as a function of pond depth. The melt pond albedo (figure 3.10) shows a large decay in the first 10-20 cm of pond depth and is relatively constant for deeper melt ponds.

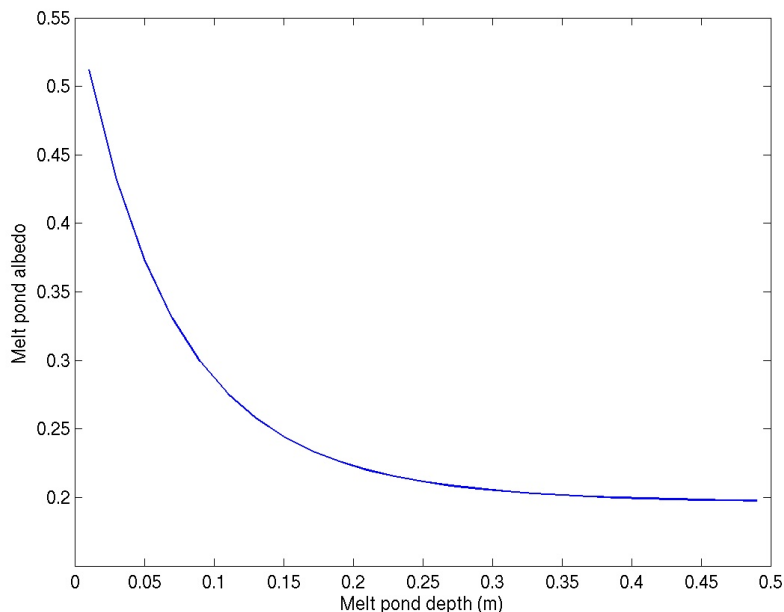


Figure 3.10: Melt pond albedo as a function of melt pond depth (based on *Schramm et al.* (1997))

During SHEBA melt ponds formation started on 11 June 1998 whereas snow started melting on 27 May (*Perovich et al.*, 2002a). Snow melt water accumulated during 14 days before pond formation started with direct effect on area-average albedo. Therefore during 14 days melt water was accumulated at the base of the snowpack but was not exposed in the form of low-albedo melt ponds. The total volume of melt water (accumulated at the surface+ drained out+ rain) produced between 27 May and 11 June is equal to 0.105 m. We assume that ponds formation start when the total volume of melt water (independent of melt pond parameterization) reaches a threshold value equal to 10.5 cm or when snow is totally removed. This threshold volume is equivalent to melting 26.25 cm of snow with a density of $400 \text{ kg}\cdot\text{m}^{-3}$. Initial melt ponds volume is set to the value given by BA08 modified since snow melting has started.

Table 3.3 describes the albedo scheme where ice surface is divided in three types: snow, ice and melt ponds and describes how the values for each surface are combined to get an area-average albedo.

Surface type	Albedo Value
Snow	α_s : evolution based on <i>Douville et al. (1995)</i> $\alpha_{s,min} = 0.72$ and $\alpha_{s,max} = 0.85$
Sea Ice	$\alpha_{ice} = \begin{cases} \min(0.73, 0.08 + 0.44h_i^{0.28}) & \text{if } T_{surf} < T_{im} \\ \min(0.5, 0.08 + 0.44h_i^{0.28}) & \text{if } T_{surf} = T_{im} \end{cases}$ $T_{im} = 273.05K$
Melt ponds	α_{pond} : depends on melt pond depth (Based on <i>Schramm et al. (1997)</i>)
Area average albedo	$\alpha = f_p \alpha_{pond} + (1 - f_p) (f_{snow} \alpha_s + (1 - f_{snow}) \alpha_{ice})$ with f_p determined according to BA08 modified and $f_{snow} = h_s / (h_s + 0.02)$

Table 3.3: Description of new sea ice albedo parameterization including melt-ponds

3.4.2 Comparison with observations

The albedo evolution is simulated with the parametrization described in table 3.3 and compared with observations from the SHEBA albedo line. The simulated albedo shows a good agreement with the observations (figure 3.11). The slow and steady decline in albedo (July 1 to August 13) is well represented. The melt ponds parameterization simulates satisfyingly this period when the melt ponds grow deeper and larger in areal extent but does not include the sharp drop in albedo associated with the appearance of melt ponds (June 12 to June 17). The increase in average albedo after mid-August due to small snow fall is not reproduced. This may arise from a too slow decrease in melt-pond fraction during the freeze-up. The simulated albedo returns to the spring time value of 0.8 by the end of September.

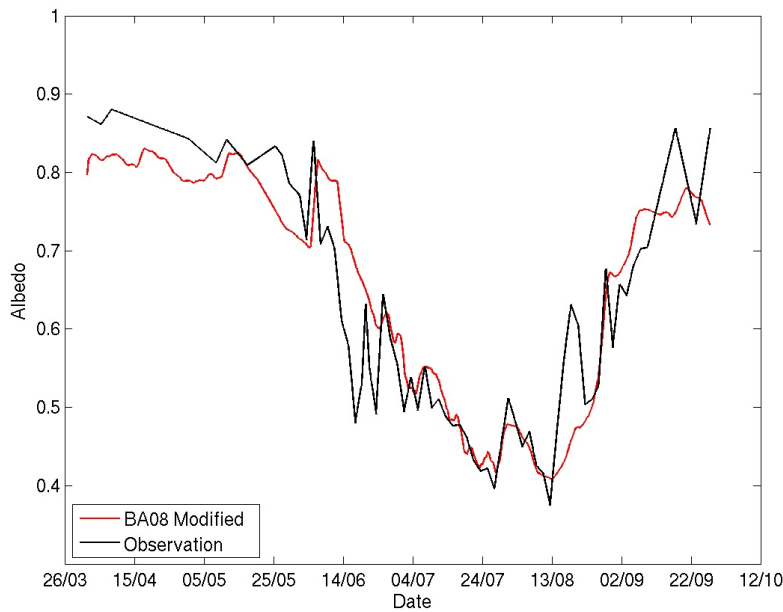


Figure 3.11: Comparison of parameterized albedo BA08 modified versus observed surface albedo. Solid black line represents the observed albedo and colored line the parameterized albedo.

3.5 Simulations results

3.5.1 Configuration

The albedo parameterization is implemented in ICESTATE. For each ice category the pond volume evolution is computed. The pond depth cannot exceed 50% of the ice thickness. When this limit is reached, ponds spread horizontally. Ponds are removed from the ice surface when ice thickness decreases below 10 cm.

3.5.2 Effects on the sea ice cover

Chapter 4

Snow heterogeneities over a grid cell

Snow plays two important but somewhat conflicting roles in the energy balance of the ice-covered Arctic Basin. On one hand, due to its high albedo, it reflect up to 85% of the incoming shortwave solar radiation, significantly retarding melting in the spring. On the other hand, because it is an excellent thermal insulator, snow decreases the rate of sensible heat loss from the ocean and ice reducing ice growth. The snow cover is not uniform and is strongly related to the age and character of the ice (e.g. *Sturm et al. (2002a); Iacozza and Barber (1999)*). On first year ice, the older is the ice the more time snow has to accumulate and the deeper it gets. Deeper snow can be found also on rougher ice that traps wind-blown snow. The snow distribution has a impact on the heat transfer from the ocean to the atmosphere during the winter. Areas with thin snow release a large amount of oceanic heat during the winter in contrast to areas with thicker snow. Snow cover heterogeneities complicates also the interpretation of sea ice remote sensing, in particular from passive microwave data.

A model including snow cover heterogeneities, initially developed for climate model, is adapted for snow on sea-ice. Snow depth measurements from several campaigns in the Arctic are compiled to get typical distribution of snow on sea ice. Its spatial and temporal evolution is considered.

4.1 SSNOWD: a representation of snow cover heterogeneities

To account for subgrid snow heterogeneities in climate model *Liston (2004)* developed the model SSNOWD (Subgrid SNOW Distribution). It aims at representing regional and global scale heterogeneous snow cover. *Liston (2004)* identified three mechanisms that are primarily responsible for spatial snow depth variation over land: 1) snow canopy interactions in forested regions, 2) snow redistribution by wind, and 3) orographic influences on solid precipitations. These factors operate at scale from tens of meters to few kilometers. It should be noticed that the variables determining snow distribution differ significantly between a terrestrial landscape and an icescape.

Snow accumulation processes The model assumes that the snow-depth distribution patterns are time invariant for a given location. That is to say that all solid precipitation reaching the surface accumulates following a subgrid snow distribution that is invariant with total accumulation value. This distribution is represented with a probability density function (PDF) that has no temporal evolution. Based on results from fieldworks *Liston (2004)* assumes that snow depth (D) distribution $f(D)$ can be described by a two-parameter lognormal PDF:

$$f(D) = \frac{1}{D\zeta\sqrt{2\pi}} \exp \left\{ -\frac{1}{2} \left[\frac{\ln(D) - \lambda}{\zeta} \right]^2 \right\} \quad (4.1)$$

with

$$\lambda = \ln(\mu) - \frac{1}{2}\zeta^2, \quad (4.2)$$

$$\zeta^2 = \ln(1 + CV^2), \quad (4.3)$$

where D is snow depth, and λ and ζ are distribution parameters related to the mean, μ , and coefficient of variation CV (equal to the ratio of the standard deviation, σ , to the mean, μ) of the snow distribution under conditions of 100% grid-cell coverage (no melting has occurred).

μ is the mean accumulated snow depth on the ground over a grid-cell and can be calculated from the solid precipitation given by an atmospheric model. CV is a parameter that defines the shape of the snow depth distribution. Figure 4.1 shows an example of snow depth distribution at different times during snow accumulation period.

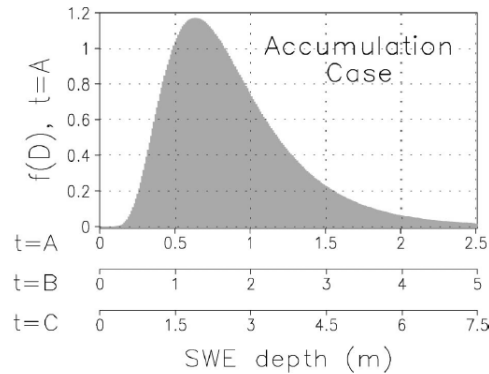


Figure 4.1: Evolution of snow distribution during the accumulation period: the shape has no temporal evolution and the cell-mean snow depth increase with time (0.9, 1.8 and 2.7 m at time A, B and C), from *Liston* (2004)

Snow ablation processes During the melting period, SSNOWD is based in simple term on the assumption that the shallowest snow disappears first, while the deepest disappears last. The snow depth distribution at the beginning of the melt period is therefore used as boundary condition that persists during the melt period. SSNOWD assumes that the melt rate over the snow-covered fraction in each grid cell is uniform and an accumulated melt depth D_m is calculated. The snow distribution shifts to the left in correspondence with D_m and creates a snow-free fraction.

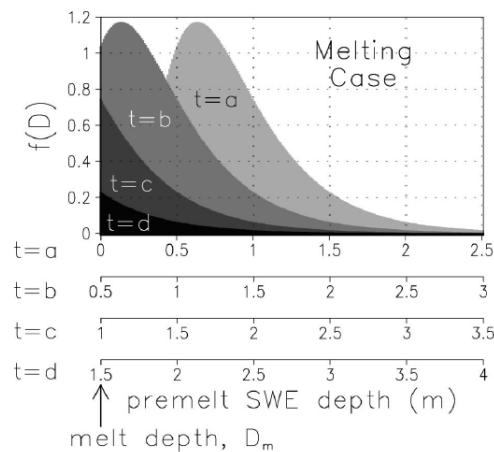


Figure 4.2: Evolution snow depth distribution with increasing snow melt depth. Distribution at $t=a$ is the pre-melt distribution, from *Liston* (2004)

Figure 4.2 illustrates this evolution where the distribution is shifted to the left by the accumulated melt depth at different times ($t=a,b,c,d$).

For a given melt depth D_m over a model grid cell, the snow covered fraction $\Gamma(D_m)$ is given by:

$$\Gamma(D_m) = 1 - \int_0^{D_m} f(D)dD \quad (4.4)$$

In SSNOWD the snow cover fraction depends on the melt depth and on the shape of the distribution (defined by CV). A formulation similar to what is used in many GCM (for a review of different snow cover fractions in climate models see *Pedersen and Winther (2005)*) is not required. Using the log-normal distribution given by equation 4.1, the snow cover fraction can be analytically calculated:

$$\Gamma(D_m) = \frac{1}{2} \operatorname{erfc} \left(\frac{z_{D_m}}{\sqrt{2}} \right) \quad \text{with} \quad z_{D_m} = \frac{\ln(D_m) - \lambda}{\zeta} \quad (4.5)$$

and the average depth D_a over a grid cell experiencing a snowmelt depth D_m is given by (see *Liston (2004)* for mathematical details) :

$$D_a(D_m) = \frac{1}{2} e^{(\lambda + \zeta^2/2)} \operatorname{erfc} \left(\frac{z_{D_m} - \zeta}{\sqrt{2}} \right) - D_m \Gamma(D_m) \quad (4.6)$$

During the spring new accumulation of snow can interrupt snowmelt. The new accumulation of snow is used to decrease melt depth value, increasing the snow cover fraction back toward 100%. If the snow melt has been reduced to zero, any additional accumulation is added to the snow depth value.

4.2 Snow-depth distribution on sea-ice

SSNOWD assumes a lognormal distribution for snow depth that is invariant for a given location. Before implementing this model to represent snow cover on sea ice the assumptions of a two-parameter lognormal distribution must be evaluated. Typical distributions of snow on sea ice must be identified.

Several datasets of snow cover on sea ice are available and are used for this evaluation.

4.2.1 Global distribution

SHEBA From early April and to mid-May 1998 extensive measurements of the snow physical characteristics and distribution were made around the SHEBA camp. Snow depths were collected along lines radiating 2 to 20 km from the ship on all types of ice. The results are reported in *Sturm et al. (2002a)*. Combining 21,169 measurements of snow depth, the mean depth was 33.7 cm with a standard deviation of 19.3 cm (figure 4.3).

The depth measurements can be reasonably described by a lognormal distribution function with $CV=0.69$. The lognormal cumulative distribution function is close to the empirical cumulative distribution function (figure 4.3 (b)).

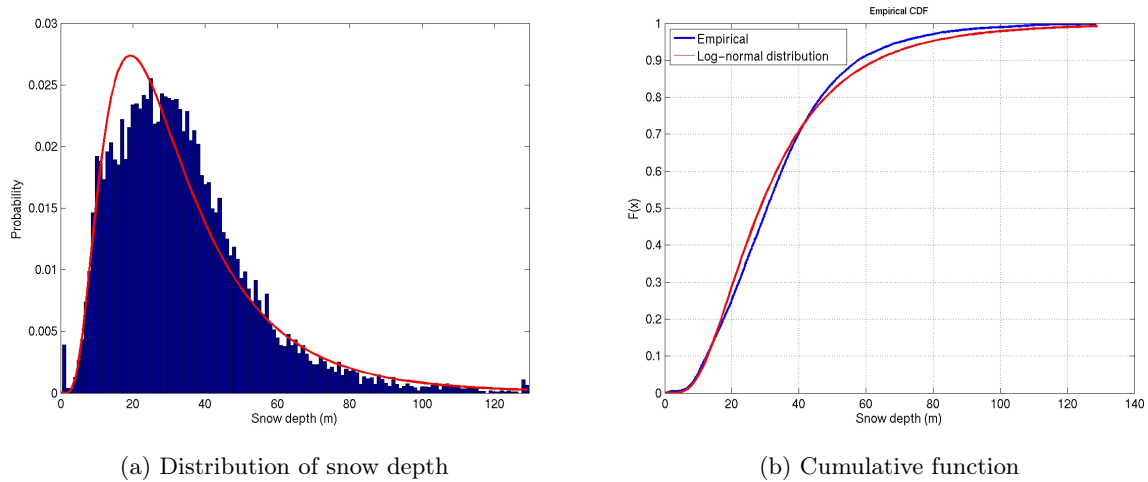


Figure 4.3: Snow depth measurement from SHEBA camp. Curve in red refers to fitted lognormal distribution

CHINARE 2003 The Chinese National Arctic Research Expedition (CHINARE) was carried out in 2003. An ice camp was deployed in the Chuckhi Sea for two weeks (22 August to 3 September). Snow depth was measured daily at random locations around the camp (*Cheng et al., 2008*). The mean snow depth is 26.5 cm with a standard deviation of 11.1 cm (figure 4.4).

The fitted lognormal distribution has a coefficient of variation equal to 0.46. However the agreement between empirical and lognormal cumulative distribution function (figure 4.4 (b)) is not as good as for SHEBA. It may come from the fact that the dataset from SHEBA contains a significantly higher number of measurements than CHINARE (21,169 against 224).

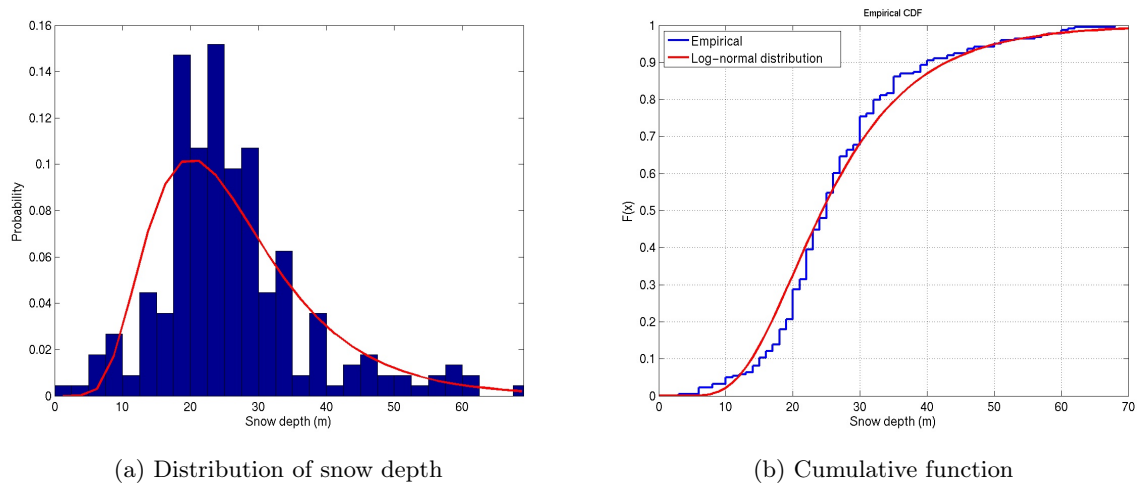


Figure 4.4: Snow depth measurement from CHINARE camp. Curve in red refers to fitted lognormal distribution

The snow distribution on sea ice can be reasonably described by a two-parameter log-normal distribution. However CV value can change. *Sturm et al. (2002a)* identified that the PDF for all depths shown in figure 4.3 can be considered as a composite of distinct PDF's from several different types of ice. The data from CHINARE 2003 and SHEBA were collected at different period of the year and represent different period in the snow cover evolution: snow accumulation during the fall for CHINARE 2003 and

pre-melt condition for SHEBA. The influence of ice type on CV and its eventual temporal evolution is evaluated in the next section.

4.2.2 Temporal and spatial evolution

Canadian Archipelago Snow depth measurements were collected during two campaigns in the Canadian Arctic in 1995 and 1996. The distribution patterns of snow over first year, multiyear and rubble sea-ice were evaluated at 15 sites. *Iacozza and Barber (1999)* used those data to develop variograms that represent the statistical pattern of the snow distribution.

The snow depth measurements for each site are gathered and a statistical analysis is performed. Histograms of snow depth and best-fitted log-normal PDF are given in appendix A. On the contrary to a variogram PDF does not include information on the spatial continuity of snow depth. Statistics on the snow distribution pattern illustrate the similarities and the differences for each site (Table 4.1).

	FYI 1	FYI 2	FYI 3	FYI 4	FYI 5	SFYI 1	SFYI 2	SFYI 3
Year	1996	1996	1996	1996	1996	1995	1995	1995
Mean (cm)	23.3	21.7	36.1	29.7	35.9	11.2	20.8	51.4
Std. dev. (cm)	7.5	6.8	7.3	7.2	7.5	6.7	11.1	21.6
CV (logn PDF)	0.34	0.36	0.22	0.23	0.22	0.68	0.73	0.60
	MYI 1	MYI 2	MYI 3	MYI 4	SMYI 1	RI 1	RI 2	
Year	1996	1996	1996	1996	1995		1996	1996
Mean (cm)	25.6	46.6	36.5	35.4	23.2		37.2	71.3
Std. dev. (cm)	15.9	21.0	18.6	19.1	16.4		24.9	31.8
CV (logn PDF)	0.95	0.60	0.72	0.85	1.22		1.07	0.69

Table 4.1: Statistics for snow cover on different sea-ice classes. CV refers to the coefficient of variation for the best-fitted log-normal law. Sites sampled in 1995 have a name with 'S' added to the ice type.

The snow distribution changes with ice type. The average snow depth is higher for rubble ice, followed by MYI and then FYI. Ice with an irregular topography is associated with higher snow depth since snow can be captured by the large uplifted ice pieces in the case of rubble ice or large rounded hummocks for MYI. FYI forms later in the season and late summer and early fall snowfall do not accumulate on the ice. The fitted log-normal distribution shows on average higher CV for irregular ice types (MYI and RI) than for flat ice (FYI). Over FYI snow distribution occurs mainly in the form of sastrugis or dunes created by the wind. Over MYI or RI snow can be deposited or eroded by the wind around ice topography, leading to a more irregular snow pattern.

Within an ice type, snow distribution can change a lot. The variation in CV within each of the ice types refers to natural variation in the spatial patterns of the snow distribution. For FYI, CV ranges from 0.22 to 0.36 in 1996 and 0.6 to 0.73 in 1995. The sites in 1996 were sampled almost one month later than in 1995 on a greater area (50 m \times 50 m in 1995 and 100 m \times 100 m in 1996). Snow had more time to accumulate in 1996 leading to a deeper and more regular snow pack. In 1996 the log-normal PDF gives a good fit of the snow distribution. For MYI and RI snow distribution changes from a site to another mainly due to the difference of ice topography.

The log-normal law gives a satisfyingly fit of the snow distribution when snow depth measurements are combined by ice types (figure 4.5). This combination may be more representative of the snow distribution at a scale larger than the sampling area.

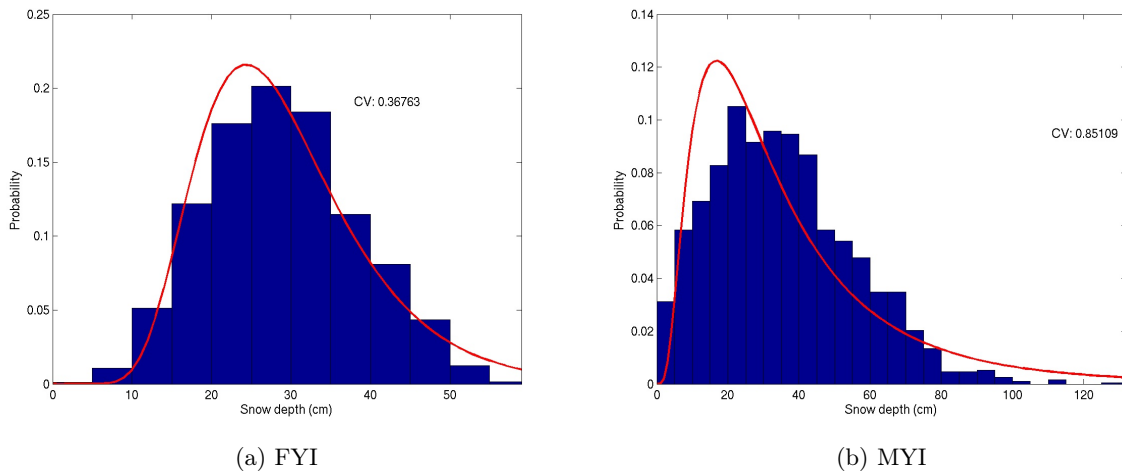


Figure 4.5: Histogram of snow depth for FYI and MYI in 1996. Red line represents the best-fitted log-normal distribution

Snow distribution over sea ice change depending on the ice topography. The more irregular is the ice topography, the more irregular is the snow pattern. Within each of the ice types large variation of CV are observed even if the sites sampled were located in the same area.

SHEBA Studies of snow cover on sea ice were carried out during the SHEBA campaign. They include an intensive campaign in April/May 1998 and a survey of snow cover evolution along several snow lines from October 1997 to October 1998.

The intensive campaign produced the histogram shown figure 4.3. As mentioned in *Sturm et al.* (2002a), it can be considered as a composite of distinct PDF's from several different types of ice. Four classes of ice were defined by *Sturm et al.* (2002a): (1) smooth ice (undeformed FYI), (2) MYI containing large refrozen melt ponds and slightly rougher FYI, (3) hummocky MYI, (4) deformed ice (rubble field and ridges). For each site of the intensive campaign where the ice type was determined, CV is calculated for the best-fitted log-normal PDF. The average value of CV are given as a function of ice type in Table 4.2.

Ice type	Undeformed FYI	Regular MYI	Hummocky MYI	Deformed ice
Numb. of sites	4	10	7	9
Max CV	0.49	1.05	1.10	1.17
Min CV	0.30	0.32	0.35	0.42
Average CV	0.39	0.53	0.53	0.70

Table 4.2: CV value as a function of ice type during the April/May campaign at SHEBA

Results are similar to those obtained in the Canadian Archipelago with a CV increasing with ice deformation but no significant difference are observed for ice classes (2) and (3) as noted by *Sturm et al.* (2002a). Large variations of CV are observed within each of the ice classes.

Those results shows the snow distribution in late April/early May, a few weeks before the onset of melting. To follow the spatial and temporal evolution of snow depth during the winter five surveys lines

were laid out. Snow depth was measured along this lines every 1 or 2 weeks from October through May and 1 or 2 days from June through August. The lines covered different types of ice (Table 4.3).

Line	Length (m)	Properties
Mainline	500	Multi-year ice
Atlanta	200	Flat ice with a small ridge at the beginning
Tuk	200	Ridged and deformed multi-year ice
Baltimore	200	First-year ice
Cleveland	200	Old eroded rubbled field (abandoned in January 98 since ice broke)

Table 4.3: Snow survey lines during SHEBA

CV along three out of four survey lines increased on average during the winter 97/98 (figure 4.6). Snow distribution change during the winter and tends to become more irregular. This may be explained by an evolution of the ice topography due to ice motion (formation of ridge, opening of leads) and by changing meteorological condition such as intense winds increasing snow redistribution. Baltimore is the exception with a CV decreasing on average during the winter.

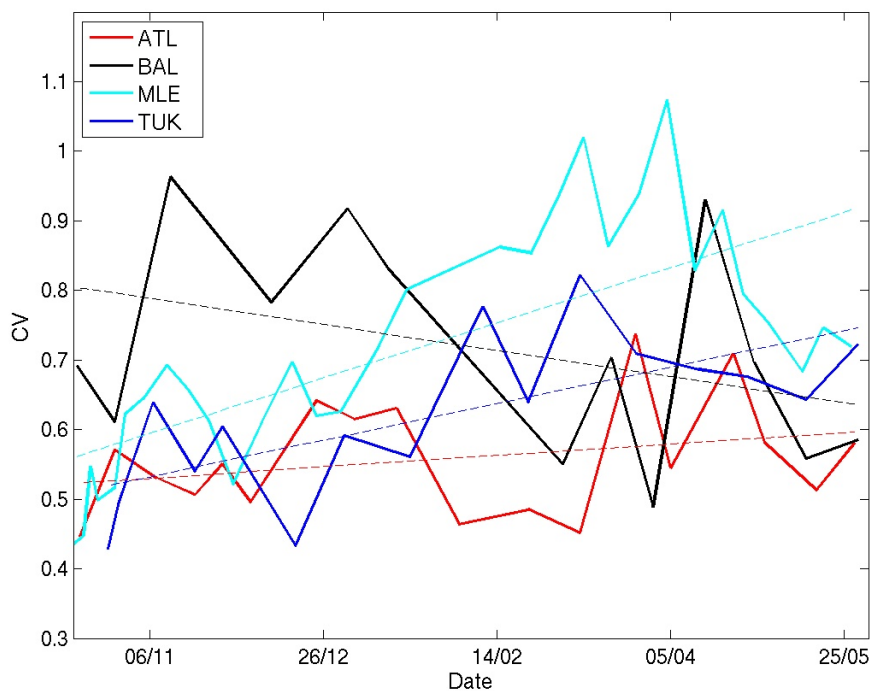


Figure 4.6: Evolution of CV along four snow lines during the winter 97/98 at SHEBA. Dashed lines represent linear trend. Results for Cleveland are not presented since ice broke in January 98

This evolution of CV at small scale (a few hundreds of meters) compared to the model scale (a few tens of kilometers) is hard to describe with accuracy. Both meteorological conditions and ice topography play a role in the snow distribution evolution. In a first approximation we decide to assume that CV is constant during the winter and that its values just depends on the ice type. The simulation of the snow

cover evolution over a parcel of sea ice with a blowing snow model such as PIEKTUK-TUVAQ (*Déry and Tremblay, 2004*) could be a solution to estimate with more accuracy the seasonal change of CV and to develop a parametrization based on wind speed, ice roughness,...

4.3 Implementation of SSNOWD in a sea-ice model

As shown in the previous section, the snow distribution over sea ice depends on the ice type. We decide to use the sea-ice model ICESTATE that includes several ice categories. Since the seasonal evolution of CV cannot be represented, we decide that each types of sea-ice has a given CV whose value is based on observations. The snow component of ICESTATE is modified to include SSNOWD.

4.3.1 SSNOWD in the snow component of ICESTATE

The description of the snow layer in ICESTATE is based on *Douville et al. (1995)* with prognostic equation for the snow albedo and the snow density. It is the same as the snow component implemented in GELATO (*Salas-Mélia, 2002*). In its default version ICESTATE saves at each time step the snow depth, density and albedo. SSNOWD requires to add two variables: the accumulated snow depth (μ) and the total snow melt depth (D_m). The area-weighted accumulated snow depth and the area weighted snow melt depth are conserved under horizontal transport and advected using WENO (see section 2.2).

When snow density increases (due to compaction or liquid precipitation over the snow cover), the snow depth is reduced to conserve snow water equivalent. The same adjustment is applied to μ and D_m and allows to conserve a constant snow cover fraction when snow density increases. Even if SSNOWD represent snow heterogeneities we assume that the snow compaction rate is uniform over a grid cell and does not depend on the snow depth.

ICESTATE includes the formation of snow ice which takes place when the snow layer part of a floe gets heavy enough to depress the ice-snow interface under the water level. Part of the snow is converted to sea ice to conserve hydrostatic balance. The snow depth is therefore reduced and snow melt depth is adjusted accordingly. Bare ice is formed in regions where the snow cover has been totally infiltrated by sea water which has frozen.

ICESTATE simulates the sea-ice dynamics and includes a rafting and ridging routine. When rafting or ridging occurs the overlying snow cover keeps the same properties. The snow thickness, μ and D_m remain the same as that over the original sea ice type. The rest of snow is compacted to ice and incorporated to the ice layer to conserve mass. The snow cover fraction is also conserved.

4.3.2 Snow distribution on different ice types

ICESTATE with 5 ice categories (see table 4.4) is used. As illustrated in 4.2, CV depends on the ice type (FYI, MYI, deformed ice). The ice age is not computed by the model which does not make distinction between ice that has undergone ridging and level ice. Therefore the ice type can be distinguished only by using different ice categories. Based on the results from SHEBA (table 4.2) and confirmed by the observations from *Iacoza and Barber (1999)* a value of CV is affected to each ice category:

Ice category	1	2	3	4	5
Upper ice category limits (m)	0.5	1.0	2.0	5.0	∞
CV	0.40	0.40	0.53	0.53	0.7

Table 4.4: Ice categories properties. CV is the coefficient of variation of the log-normal distribution of snow depth

4.3.3 Albedo formulation

Snow plays a great role in the surface budget of sea ice. Due to its high albedo snow tends to delay the onset of ice melt. Once the snow melt has started the ice surface is composed of bare ice, snow covered ice and ponded ice (e.g. *Perovich et al. (2002a)*). The area-average albedo is a combination of the albedo of each patch. Based on SSNOWD the snow covered fraction $\Gamma(D_m)$ is computed. The average albedo of the ice covered part is then:

$$\alpha = \Gamma(D_m)\alpha_s + (1 - \Gamma(D_m))\alpha_{ice} \quad (4.7)$$

where α_s is the prognostic snow albedo based on *Douville et al. (1995)* and α_{ice} the ice albedo that depends on surface temperature and ice thickness (melt ponds are not yet represented).

The snow cover fraction depends on the accumulated depth, the melt depth and the shape of the distribution (defined by CV).

4.3.4 Effect on heat transfer

Due to its low thermal conductivity the snow cover increases in winter the insulation of the atmosphere from the relatively warm ocean and decreases the ice growth. The snow depth, its metamorphic state and its areal distribution impact heat flow through the ice and therefore the rate of ice growth (*Sturm et al., 2002b*). In this part we focus on the impact of the snow aerial distribution.

Sturm et al. (2002b) and *Sturm et al. (2001)* showed that the winter heat flux at SHEBA had an high spatial variability with the presence of concentrated "hot spots" at the surface where the rate of heat loss was much higher than elsewhere. They were associated with regions of thin snow. Convolving a heat flow versus depth function with a snow depth distribution function around SHEBA (figure 4.3) *Sturm et al. (2002b)* determined the enhancement in heat flow due to "hot spots". The flux from the heterogeneous snow cover was 1.4 times greater than the flux from a homogeneous snow cover. This enhancement is associated with nonvertical transfer of heat due to ice and snow geometry.

The parameters of the snow distribution given by SSNOWD are combined to compute an enhancement factor that accounts for the snow heterogeneities for a given ice category. This is done in a similar way to *Fichefet and Maqueda (1997)* who introduced in their mono-category sea ice model a correction factor that accounts for the thermodynamics effect of the subgrid-scale snow and ice thickness distribution. In ICESTATE we introduce a factor that correct the surface heat flux according to the snow distribution.

In ICESTATE the conductive heat flux is treated in two different ways depending on a user-defined ice thickness h_L . For thin ice ($h < h_L$) the ice has a linear temperature profile. For ice of thickness greater than h_L the heat equation is solved in the ice slab using a finite difference scheme. Therefore the surface heat flux is expressed in two different ways:

$$F_c = \begin{cases} \frac{k_s k_i}{h_i k_s + D_a k_i} (T_f - T_{surf}) & \text{for thin ice} \\ \frac{k_s k_i}{\frac{h_i}{2N} k_s + D_a k_i} (T_{i,N} - T_{surf}) & \text{for thick ice (N layers)} \end{cases} \quad (4.8)$$

where k_s and k_i are the snow and ice conductivity, D_a and h_i the snow depth and ice thickness. T_{surf} is the surface temperature, T_f the temperature at the freezing point of sea water and $T_{i,N}$ the temperature of the top ice layer (whose thickness is h_i/N). The only difference is that in the thin ice case the ice bottom surface is used at the lower interface whereas the midpoint of the top layer is used in the case with thick ice.

For a given snow distribution the heat flux average over all the snow depth D can be computed as:

$$F_{tot} = (1 - \Gamma(D_m))F_{ice} + \int_{D_m}^{\infty} F_c(D - D_m)f(D)dD \quad (4.9)$$

where $f(D)$ is the snow depth PDF and F_{ice} the conductive heat flux through bare ice. This expression is simplified when the grid cell is totally covered by snow: $F_{tot} = \int_0^{\infty} F_c(D)f(D)dD$.

In 4.8 T_{surf} and $T_{i,N}$ depend on the snow depth and the ice thickness. By assuming a linear temperature profile in the ice, even for thick ice, we get a simplified expression for F_c that is suitable for both thin and thick ice:

$$F_c = \frac{k_s k_i}{h_i k_s + h_s k_i} (T_f - T_{surf}) \quad (4.10)$$

Following *Fichefet and Maqueda (1997)* we introduce an effective thickness for the snow-ice system, $D_l = [k_s k_i / (k_s + k_i)] (D_a - D_m / k_s + h_i / k_i)$. Under horizontally homogeneous atmospheric and oceanic condition *Fichefet and Maqueda (1997)* showed that the surface temperature T_{surf} is nearly the same whatever the snow depth and ice thickness, provided that the effective thickness is larger than a certain threshold $\epsilon = 0.1$ m. In the range $0 < D_l < \epsilon$, T_{surf} varies linearly with D_l between T_f and T_{surf}^* , the surface temperature for $D_l > \epsilon$.

The minimum effective thickness is given by: $D_{l,min} = [k_s / (k_s + k_i)] h_i$. According to the value of $D_{l,min}$ two cases must be considered. If $D_{l,min} > \epsilon$ the surface temperature is constant equal to T_{surf}^* everywhere. In the second case, if $D_{l,min} < \epsilon$ a fraction of the grid cell has a surface temperature between T_f and T_{surf}^* .

We define a conduction correction factor G such as $F_{tot} = G \frac{k_s k_i}{h_i k_s + D_a k_i} (T_f - T_{surf}^*)$. In the case $D_{l,min} > \epsilon$ equation 4.9 implies that:

$$G = \left(D_a \frac{k_i}{k_s} + h_i \right) \left[\frac{1}{h_i} (1 - \Gamma(D_m)) + k_s \int_{D_m}^{\infty} \frac{1}{k_i (D - D_m) + k_s h_i} f(D) dD \right] \quad (4.11)$$

When $D_{l,min} < \epsilon$ we note ϵ_s the snow depth for which $D_l = \epsilon$: $\epsilon_s = D_m + \epsilon(1 + k_s/k_i) - h_i k_s/k_i$. Therefore the correction factor is given by:

$$G = (D_a k_i + h_i k_s) \left[\frac{1 - \Gamma(\epsilon_s)}{(k_s + k_i)\epsilon} + \int_{\epsilon_s}^{\infty} \frac{1}{k_i (D - D_m) + k_s h_i} f(D) dD \right] \quad (4.12)$$

The integrals in 4.11 and 4.12 cannot be solved analytically. A numerical approximation is computed thanks to the Simpson's method. The conduction correction factor G depends on CV , the ice thickness, the average snow depth and the melt depth. Figure 4.7 shows the evolution of G when no melting has occurred ($D_m = 0$ m). For a given average snow depth G decreases with the ice thickness since higher is the ice thickness, lower is the influence of the snow cover on the heat transfer (Figure 4.7 (a)). For thick snow cover G is higher than for thin snow cover (Figure 4.7 (b)). The same evolution is observed when CV increases. The effects of the snow heterogeneities on the heat transfer are more sensitive when the snow depth is higher and the snow distribution is less uniform.

ICESTATE includes a thermal inertia heat flux F_{inrt} . This is a simple parameterization of ice heating. Indeed as the surface temperature of the ice is changing, some of the heat flux going into the ice will change the ice temperature. This parameterization ensures a smooth evolution of the surface temperature. It assumes that snow has zero heat capacity.

ICESTATE uses this parameterization for the total ice slab for thin ice and for the top half of the uppermost ice layer for thick ice. The correction factor G modifies the expression of F_{inrt} and accounts for snow heterogeneities effect on the heat transfer:

$$F_{inrt} = \begin{cases} -c_{pi} \rho_i h_i G \frac{k_s h_i}{2(h_i k_s + D_a k_i)} \frac{\partial T_{surf}}{\partial t} & \text{for thin ice} \\ -c_{pi} \rho_i G \frac{h_i}{2N} \frac{k_s h_i / 2N}{2(k_s h_i / 2N + k_i D_a)} \frac{\partial T_{surf}}{\partial t} & \text{for thick ice (N layers)} \end{cases} \quad (4.13)$$

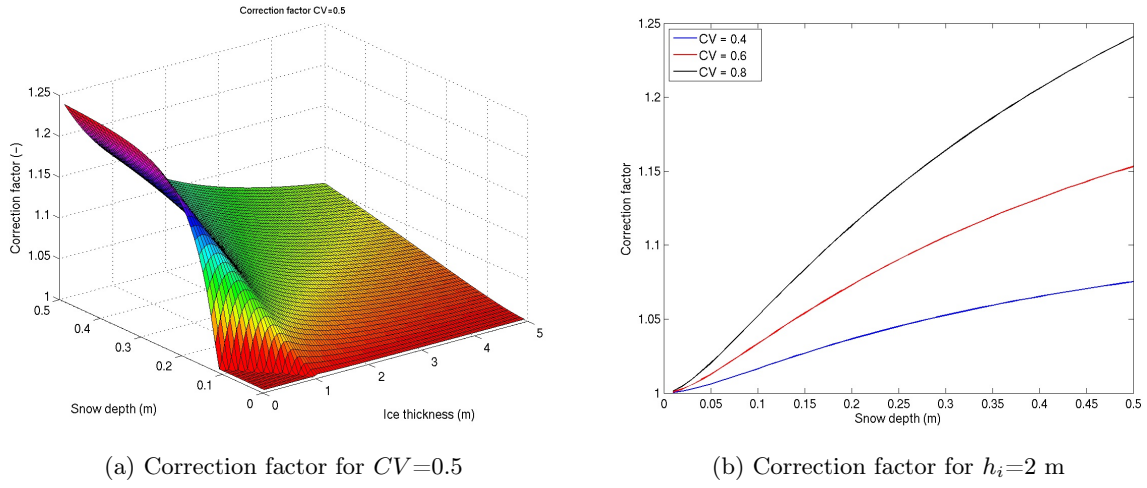


Figure 4.7: Evolution of the conduction correction factor G when the ice is 100 % snow-covered ($D_m=0$ m). The formation of snow-ice is not considered in (a).

$$\int_{D_m}^{\infty} \frac{1}{k_i(D - D_m) + k_s h_i} \frac{1}{D \zeta \sqrt{2\pi}} \exp \left\{ -\frac{1}{2} \left[\frac{\ln(D) - \lambda}{\zeta} \right]^2 \right\} dD$$

Appendix A

Snow depth distribution (from *Iacozza and Barber (1999)*)

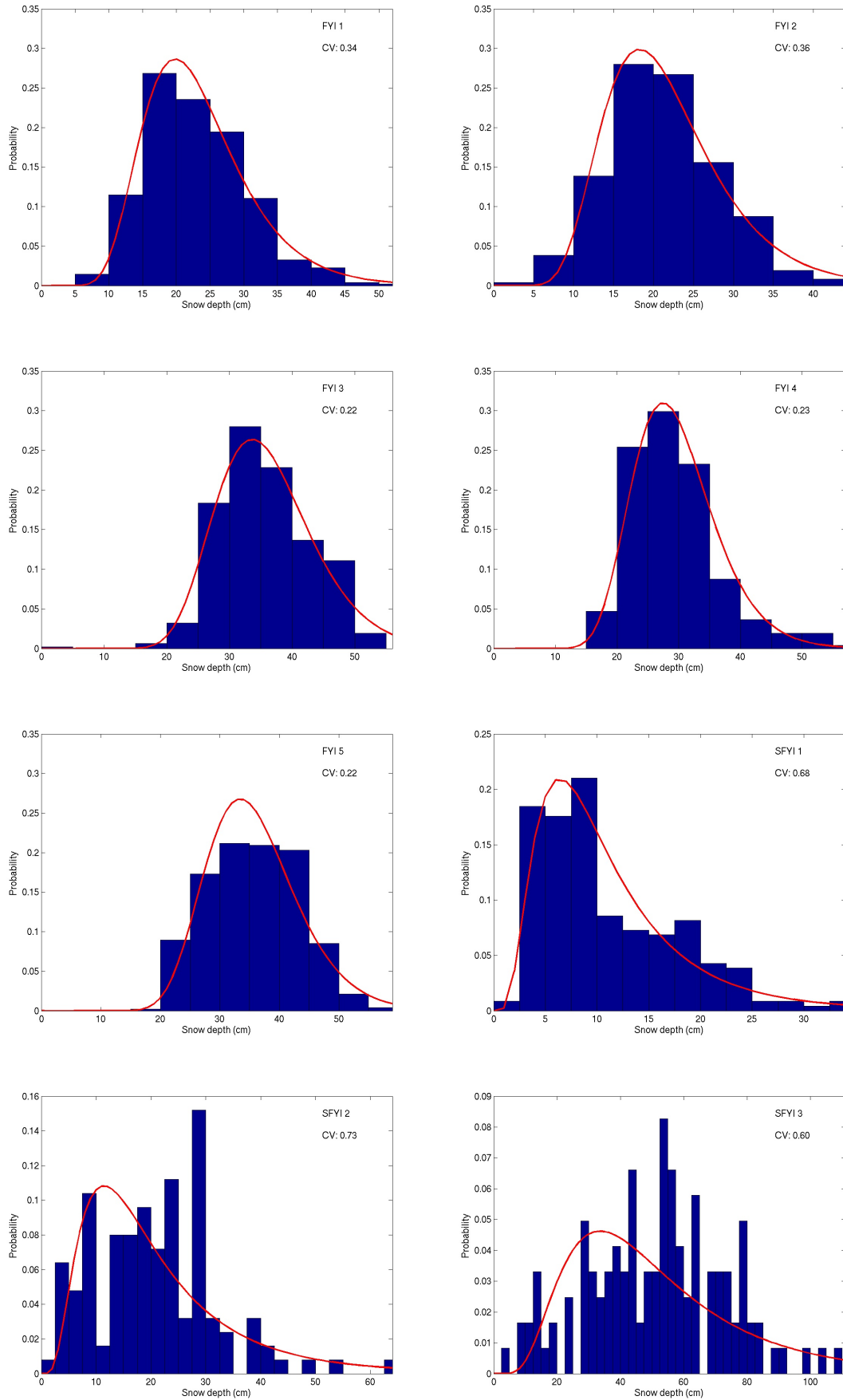


Figure A.1: Histogram of snow depth for first-year ice at 7.5 sites. Red line represents the best-fitted log-normal distribution

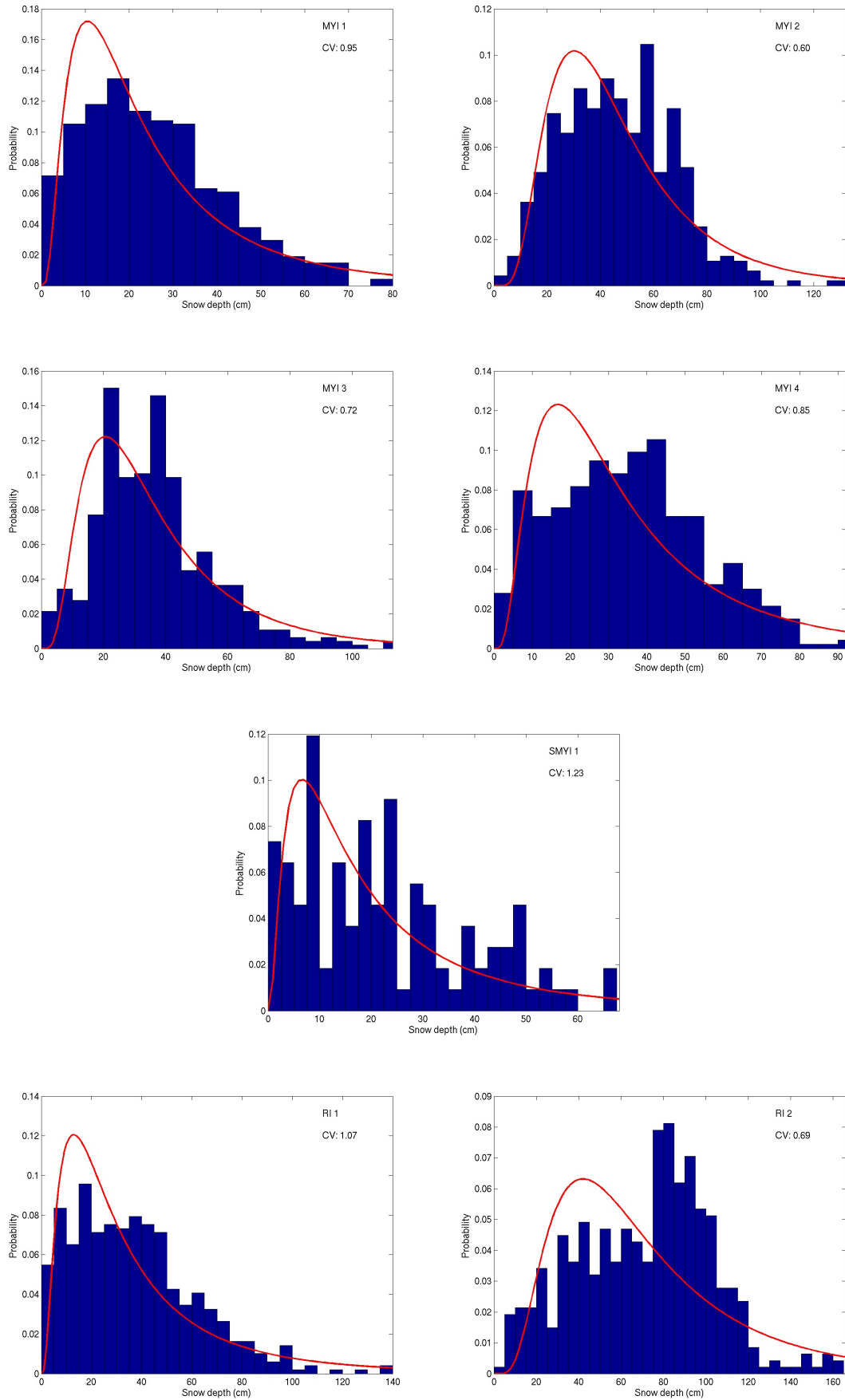


Figure A.2: Histogram of snow depth for multi-year and rubble ice at 7 sites. Red line represents the best-fitted log-normal distribution

Bibliography

- Cheng, B., Z. Zhang, T. Vihma, M. Johansson, L. Bian, Z. Li, and H. Wu (2008), Model experiments on snow and ice thermodynamics in the Arctic Ocean with CHINARE 2003 data, *J. Geophys. Res.*, 113.
- Déry, S., and L. Tremblay (2004), Modeling the effects of wind redistribution on the snow mass budget of polar sea ice, *Journal of Physical Oceanography*, 34(1), 258–271.
- Douville, H., J. Royer, and J. Mahfouf (1995), A new snow parameterization for the Météo-France climate model, *Climate Dynamics*, 12(1), 21–35.
- Drange, H., and K. Simonsen (1996), Formulation of Air-Sea Fluxes in the ESOP2 Version of MICOM, *Tech. Rep. 125*, NERSC.
- Ebert, E., and J. Curry (1993), An intermediate one-dimensional thermodynamic sea ice model for investigating ice-atmosphere interactions, *Journal of Geophysical Research*, 98(C6).
- Eicken, H., T. Grenfell, D. Perovich, J. Richter-Menge, and K. Frey (2004), Hydraulic controls of summer Arctic pack ice albedo, *J. Geophys. Res.*, 109(C08007).
- Enomoto, T. (2007), Ocean surface albedo in AFES, *JAMSTEC Rep. Res. Dev.*, 6, 21–30.
- Fetterer, F., and N. Untersteiner (1998), Observations of melt ponds on Arctic sea ice, *Journal of Geophysical Research*, 103(C11).
- Fichefet, T., and M. Maqueda (1997), Sensitivity of a global sea ice model to the treatment of ice thermodynamics and dynamics, *Journal of Geophysical Research*, 102(C6).
- Grenfell, T., and D. Perovich (2004), Seasonal and spatial evolution of albedo in a snow-ice-land-ocean environment, *Journal of Geophysical Research*, 109(C1).
- Hanesiak, J., D. Barber, and G. Flato (1999), Role of diurnal processes in the seasonal evolution of sea ice and its snow cover, *Journal of Geophysical Research*, 104(C6).
- Hunke, E., and W. Lipscomb (2008), *CICE : the Los Alamos Sea Ice Model Documentation and Software User's Manual Version 4.0*.
- Iacoza, J., and D. Barber (1999), An Examination of the Distribution of Snow on Sea-Ice, *ATMOSPHERE OCEAN*, 37, 21–51.
- Johanessen, O., E. Shalina, and C. Myrmeh (2002), AICSEX Sea Ice Concentration in the Arctic, 1978-2000, CD-ROM.
- Koltzow, M. (2007), The effect of a new snow and sea ice albedo scheme on regional climate model simulations, *J. Geophys. Res.*, 112(D7110).
- Laine, V. (2004), Arctic sea ice regional albedo variability and trends, 1982–1998, *J. Geophys. Res.*, 109.

- Lindsay, R. (2003), Changes in the modeled ice thickness distributions near the SHEBA drifting ice camp, *J. Geophys. Res.*, *108*, 3194.
- Lipscomb, W., and E. Hunke (2004), Modeling sea ice transport using incremental remapping, *Monthly Weather Review*, *132*(6), 1341–1354.
- Lisæter, K. (2007), A Coupled Ice-ocean Data Assimilation System for Arctic Monitoring and Prediction, Ph.D. thesis, Department of Mathematics, University of Bergen.
- Liston, G. (2004), Representing Subgrid Snow Cover Heterogeneities in Regional and Global Models, *Journal of Climate*, *17*(6), 1381–1397.
- Liu, J., Z. Zhang, J. Inoue, and R. Horton (2007), Evaluation of snow/ice albedo parameterizations and their impacts on sea ice simulations, *International Journal of Climatology*, *27*(1), 81–91.
- Lüthje, M., D. Feltham, P. Taylor, and M. Worster (2006), Modeling the summertime evolution of sea-ice melt ponds, *J. Geophys. Res.*, *111*.
- Maykut, G. (1982), Large-scale heat exchange and ice production in the Central Arctic, *Journal of Geophysical Research*, *87*(C10).
- Mölders, N., H. Luijting, and K. Sassen (2008), Use of atmospheric radiation measurement program data from Barrow, Alaska, for evaluation and development of snow-albedo parameterizations, *Meteorology and Atmospheric Physics*, *99*(3), 199–219.
- Morassutti, M., and E. LeDrew (1996), Albedo and depth of melt ponds on sea-ice, *International Journal of Climatology*, *16*(7), 817–838.
- Pedersen, C., and J. Winther (2005), Intercomparison and validation of snow albedo parameterization schemes in climate models, *Climate Dynamics*, *25*(4), 351–362.
- Perovich, D., T. Grenfell, B. Light, and P.V.Hobbs (2002a), Seasonal evolution of the albedo of multiyear Arctic sea ice, *J. Geophys. Res.*, *107*, doi:10.1029/2000JC000438.
- Perovich, D., W. Tucker III, and K. Ligett (2002b), Aerial observations of the evolution of ice surface conditions during summer, *J. Geophys. Res.*, *107*(8048), 10–1029.
- Perovich, D., T. Grenfell, J. Richter-Menge, B. Light, W. Tucker III, and H. Eicken (2003), Thin and thinner: Sea ice mass balance measurements during SHEBA, *J. Geophys. Res.*, *108*(10.1029).
- Perovich, D., T. Grenfell, B. Light, B. Elder, J. Harbeck, W. Polashenski, C. Tucker III, and C. Stelmach (2008), Transpolar observations of the morphological properties of Arctic sea ice, *Journal of Geophysical Research*.
- Perovich, D., et al. (1999), SHEBA. Snow and Ice Studies, CRREL, CD-ROM.
- Persson, P., C. Fairall, E. Andreas, P. Guest, and D. Perovich (2002), Measurements near the atmospheric surface flux group tower at SHEBA: near-surface conditions and surface energy budget, *J. Geophys. Res.*, *107*, doi:10.1029/2000JC000705.
- Romanov, I. (1995), *Atlas of Ice and Snow of the Arctic Basin and Siberian Shelf Seas*, 2 nd ed., Backbone, New York.
- Salas-Mélia, D. (2002), A global coupled sea ice-ocean model, *Ocean Modelling*, *4*(2), 137–172.
- Schramm, J., M. Holland, J. Curry, and E. Ebert (1997), Modeling the thermodynamics of a sea ice thickness distribution. Part 1: Sensitivity to ice thickness resolution, *J. Geophys. Res.*, *102*(23).
-

- Smolarkiewicz, P. (1984), A fully multidimensional positive definite advection transport algorithm with small implicit diffusion, *J. Comput. Phys*, *54*, 325–362.
- Smolarkiewicz, P., and T. Clark (1986), The multidimensional positive definite advection transport algorithm: Further development and applications, *Journal of Computational Physics*, *67*(2), 396–438.
- Sturm, M., J. Holmgren, and D. Perovich (2001), Spatial variations in the winter heat flux at SHEBA: estimates from snow-ice interface temperatures, *Annals of Glaciology*, *33*, 213–220.
- Sturm, M., J. Holmgren, and D. Perovich (2002a), Winter snow cover on the sea ice of the Arctic Ocean at the Surface Heat Budget of the Arctic Ocean (SHEBA): Temporal evolution and spatial variability, *J. Geophys. Res*, *107*(8047), 10–1029.
- Sturm, M., D. Perovich, and J. Holmgren (2002b), Thermal conductivity and heat transfer through the snow on the ice of the Beaufort Sea, *J. Geophys. Res*, *107*, 1–14.
- Svendsen, E., K. Kloster, B. Farrelly, O. Johannessen, J. Johannessen, W. Campbell, P. Gloerse, D. Cavalieri, and C. Mätzler (1983), Norwegian Remote Sensing Experiment: Evaluation of the Nimbus 7 Scanning Multichannel Microwave Radiometer of sea ice research, *Journal of Geophysical Research*, *88*(C5).
- Taylor, P., and D. Feltham (2004), A model of melt pond evolution on sea ice, *J. Geophys. Res*, *109*.
- Tschudi, M., J. Curry, and J. Maslanik (2001), Airborne observations of summertime surface features and their effect on surface albedo during FIRE/SHEBA (Paper 2000JD900275), *J. Geophys. Res*, *106*(14), 15–15.
- Uppala, S., et al. (2005), The ERA-40 re-analysis, *Q.J.R Meteorol. Soc.*, *107*(612), 2961–3012.
- Woodgate, R., K. Aagaard, and T. Weingartner (2005), Monthly temperature, salinity, and transport variability of the Bering Strait through flow, *Geophys. Res. Lett*, *32*.
- Xiong, X., K. Stamnes, and D. Lubin (2002), Surface Albedo over the Arctic Ocean Derived from AVHRR and Its Validation with SHEBA Data, *Journal of Applied Meteorology*, *41*(4), 413–425.
-